INL/EXT-09-16559

Long-Term Degradation Testing of High-Temperature Electrolytic Cells

C. M. Stoots
J. E. O'Brien
J. S. Herring
G. K. Housley
D. G. Milobar
M. S. Sohal
J. J. Hartvigsen
D. Larsen
S. Elangovan
Thomas Cable

August 2009

The INL is a U.S. Department of Energy National Laboratory
operated by Battelle Energy Alliance

Idaho National Laboratory

INL/EXT-09-16559

Long-Term Degradation Testing of High-Temperature Electrolytic Cells

C. M. Stoots
J. E. O'Brien
J. S. Herring
G. K. Housley
D. G. Milobar
M. S. Sohal
J. J. Hartvigsen[1]
D. Larsen[1]
S. Elangovan[1]
Thomas Cable[2]

[1]Ceramatec, Inc.
[2]NASA-Glenn

August 2009

Idaho National Laboratory
Idaho Falls, Idaho 83415

http://www.inl.gov

Prepared for the
U.S. Department of Energy
Office of Nuclear Energy
Under DOE Idaho Operations Office
Contract DE-AC07-05ID14517

Long-Term Degradation Testing of High-Temperature Electrolytic Cells

INL/EXT-09-16559
Revision 0

August 2009

Approved by:

Carl M. Stoots Principal Investigator	Date
James E. O'Brien Principal Investigator	Date
J. Stephen Herring Technical Director, High Temperature Electrolysis	Date

ABSTRACT

The Idaho National Laboratory (INL) has been researching the application of solid-oxide electrolysis cell for large-scale hydrogen production from steam over a temperature range of 800 to 900ºC. The INL has been testing various solid oxide cell designs to characterize their electrolytic performance operating in the electrolysis mode for hydrogen production. Some results presented in this report were obtained from cells, with an active area of 16 cm^2 per cell. The electrolysis cells are electrode-supported, with ~10 μm thick yttria-stabilized zirconia (YSZ) electrolytes, ~1400 μm thick nickel-YSZ steam-hydrogen electrodes, and manganite (LSM) air-oxygen electrodes. The experiments were performed over a range of steam inlet mole fractions (0.1 to 0.6), gas flow rates, and current densities (0 to 0.6 A/cm^2). Steam consumption rates associated with electrolysis were measured directly using inlet and outlet dewpoint instrumentation. On a molar basis, the steam consumption rate is equal to the hydrogen production rate. Cell performance was evaluated by performing DC potential sweeps at 800, 850, and 900°C. The voltage-current characteristics are presented, along with values of area-specific resistance as a function of current density. Long-term cell performance is also assessed to evaluate cell degradation. Details of the custom single-cell test apparatus developed for these experiments are also presented.

NASA, in conjunction with the University of Toledo, has developed a new cell concept with the goals of reduced weight and high power density. This report presents results of the INL's testing of this new solid oxide cell design as an electrolyzer. Gas composition, operating voltage, and other parameters were varied during testing. Results to date show the NASA cell to be a promising design for both high power-to-weight fuel cell and electrolyzer applications.

CONTENTS

ABSTRACT v

ACRONYMS xi

NOMENCLATURE xiii

1. INTRODUCTION 1
   1.1 INL High Temperature Electrolysis Laboratory 2

2. SOLID OXIDE CELL AND POLARIZATION LOSSES 5
   2.1 Solid Oxide Cell 5
   2.2 Polarization Losses 7

3. DEGRADATION PHENOMENA IN SOLID OXIDE ELECTROLYSIS CELLS 10
   3.1 Degradation Phenomena and Models 10

4. PERFORMANCE OF SINGLE ELECTRODE-SUPPORTED CELLS IN THE ELECTROLYSIS MODE 14
   4.1 Single-Cell Test Apparatus Design and Fabrication 14
   4.2 Cell Reduction 18
   4.3 Test Procedure and Analysis 18
   4.4 Preliminary Test Results 20
   4.5 Initial and Long-Term Performance of St. Gobain Electrode-Supported Cells 21

5. PERFORMANCE OF THE NASA BI-ELECTRODE SUPPORTED CELL 26
   5.1 Button Cell Fabrication by NASA 26
   5.2 Button Cell Test Results 27

6. INL TESTS ON DEGRADATION IN SHORT STACKS AND ILS STACKS 33

7. IMPROVED CERAMATEC CELLS 37

8. STATUS OF 2500-HR TEST OF A 10-CELL CERAMATEC STACK 38

9. STATUS OF CERAMATEC FULLY-STABILIZED ELECTROLYTE BUTTON CELL TEST 39

10. ACKNOWLEDGMENTS 40

11. REFERENCES 40

FIGURES

Figure 1-1. Schematic of HTE system coupled to an advanced nuclear reactor. 1
Figure 1-2. INL high-temperature electrolysis laboratory. 2
Figure 1-3. General schematic of one of INL solid oxide cell testing apparati. 3
Figure 2-1. (a) Solid oxide electrolytic cell (SOEC); (b) solid oxide fuel cell (SOFC) (Guan et al. 2006). 5
Figure 2-2. Ceramatec solid oxide cell/stack construction (scanning electron microscopy figure on the right is from Carter et al. 2008). 6
Figure 2-3. SOFC voltage-current characteristics for a single cell operating at 800°C (Windisch et al. 2002). 8
Figure 3-1. Operating mechanisms of solid oxide cells: (a) a SOEC in electrolysis mode, and (b) a SOFC in fuel cell mode (Ni et al. 2006). 10
Figure 3-2. TPBs in a solid oxide cell, shown as red dots, where reactions take place (Hauch 2007a). 13
Figure 4-1. Exploded view of cell test fixture. 15
Figure 4-2. (a) alumina cell holder; (b) cell holder with cell in place. 15
Figure 4-3. Alumina air flow distributor. 16
Figure 4-4. Test stand overview. 17
Figure 4-5. Test stand installed in furnace base. 17
Figure 4-6. Polarization curves for electrode-supported cell. 20
Figure 4-7. Area-specific resistance for electrode-supported cells as a function of current density. 21
Figure 5-1. Cross section of a sintered BSC cell showing the thin YSZ (white) electrolyte in the center and the YSZ scaffolds, and the micro channels (black) formed by the ice crystals during freeze-casting, and then removed during freeze drying. The bright white at the top and bottom of the cell is Au ink. 26
Figure 5-2. NASA button cell mounted on support YSZ tube. 27
Figure 5-3. Polarization curve for NASA Cell 1. 28
Figure 5-4. H_2 production rates and dew points for NASA Cell 1 (corresponding to Figure 5-3). 29
Figure 5-5. Polarization curve and respective ASR values for NASA Cell 3. 29
Figure 5-6. H_2 production rates and dew points for NASA Cell 3 (corresponding to Figure 5-5). 30
Figure 5-7. H_2 production rates and polarization curve for NASA Cell 5. 30
Figure 5-8. Polarization curves for NASA Cell 7. 31
Figure 5-9. Long duration test data for NASA cell 7. 32
Figure 6-1. Area-specific resistance of a button cell as a function of time for the 1,100-hour test. 33
Figure 6-2. Area-specific resistance of a 25-cell stack as a function of time for a 1,000-hour test. 34
Figure 6-3. Hydrogen production rates during 1,000-hour long-term test. 34

Figure 6-4. Time history of ILS module ASR values, voltages, and current over 700 hours of operation. 35
Figure 6-5. Time history of hydrogen production rate in the ILS. 36
Figure 8-1. Performance of the 10-cell Ceramatec stack through 1,500 hours. 38
Figure 1-1. Performance of the Ceramatec fully-stabilized electrolyte button cell 39

TABLES

Table 2-1. Commonly used materials in SOFC/SOEC (Gazzarri 2007) 6
Table 4-1. Cell electrode reduction procedure. 18
Table 5-1. Cell test conditions. 27

ACRONYMS

3-D	three dimensional
ASR	area-specific resistance
CFD	computational fluid dynamics
EDS	energy dispersive X-ray spectroscopy
EIS	electrochemical impedance spectroscopy
HTE	high-temperature electrolysis
ILS	integrated laboratory scale
INL	Idaho National Laboratory
LSC	lanthanum strontium chromite
LSCF	lanthanum strontium cobalt iron oxide
LSF	strontium-doped lanthanum ferrite
LSM	strontium-doped lanthanum manganite
LZO	lanthanum zirconate
Ni-YSZ	nickel-yttria stabilized zirconia
PNNL	Pacific Northwest National Laboratory
ScSZ	scandia-stablized zirconia
SDC	samaria-doped ceria
SEM	scanning electron microscopy
SOEC	solid oxide electrolysis cells
SOFC	solid oxide fuel cell
TEM	transmission electron microscopy
TPB	triple-phase boundary
YSZ	yttria stabilized zirconia

NOMENCLATURE

F	Faraday number, 96487 C/mol
ASR	area-specific resistance, Ohm·cm^2
ΔG_f	Gibbs energy of formation, J/mol
i	current density, A/cm^2
I	current, A
$\dot{N}_{H_2}$	molar hydrogen production rate, mol/s
N_{O2prod}	number of oxygen equivalents
P	pressure, kPa
q”	heat flux, W/cm^2
Q_M	molar flow rate, mol/s
Q	volumetric flow rate, sccm
R_u	universal gas constant, J/mol·K
T	temperature, K
T_{dp}	dewpoint temperature
U_{H2O}	steam utilization, %
V_N	Nernst potential, V
V_{cell}	cell operating voltage, V
V_{OC}	open-cell voltage, V
V_{tn}	thermal neutral voltage, V
y	mole fraction
ρ_M	standard-state molar density, mol/m^3

Long-Term Degradation Testing of High-Temperature Electrolytic Cells

1. INTRODUCTION

Idaho National Laboratory (INL) is performing high-temperature electrolysis (HTE) research to generate hydrogen using solid oxide electrolysis cells (SOECs). A schematic depicting a high-temperature gas-cooled reactor coupled to an HTE system is shown in Figure 1-1. This system produces hydrogen using the heat and electricity generated by a high-temperature nuclear reactor. The ~900°C primary helium coolant uses about 85% of the thermal energy output of the reactor to drive a gas-turbine Brayton power cycle, which provides the electrical energy required for the HTE process. The remaining 20% of the reactor thermal energy is used to generate steam at about 850°C. The combination of a high-efficiency power cycle and the direct utilization of nuclear process heat yields an overall thermal-to-hydrogen conversion efficiency of 50% or higher.

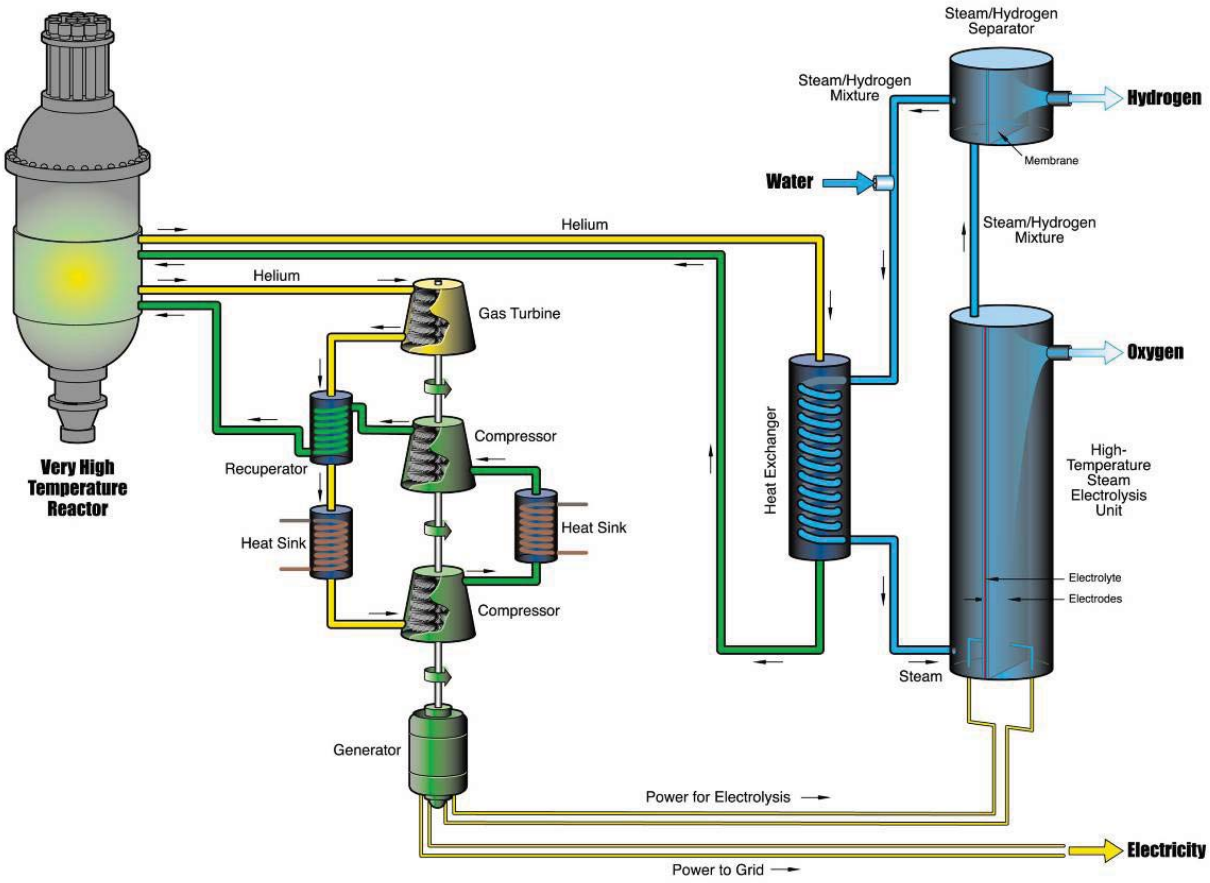

Figure 1-1. Schematic of HTE system coupled to an advanced nuclear reactor.

The objective of the INL project is to address the technical and scale-up issues associated with the implementation of SOEC technology for hydrogen production from steam. In the envisioned application, HTE would be coupled to an advanced nuclear reactor for efficient, large-scale, non-fossil, non-greenhouse gas hydrogen production. The project supports a broad range of activities, including

small bench-scale experiments, larger-scale technology demonstrations, detailed computational fluid dynamic modeling, and system modeling. For this technology to be successful in a large industrial setting, several issues related to solid oxide cells need to be resolved, including: stack design optimization, identification and evaluation of cell performance degradation parameters and processes, integrity and reliability of the SOEC stacks, lifetime prediction, and extension of the SOEC stacks. This INL project simultaneously addresses the technical and scale-up issues associated with a progression of electrolysis cell and stack testing activities at increasing scales. This report provides a summary of the cell and stack testing and their degradation. A part of this report is taken from four previous reports associated with related ongoing work on high temperature electrolysis at INL (Sohal 2009a, Sohal et al. 2009b, Stoots et al. 2009a, Hartvigsen et al. 2009, O'Brien et al. 2009a and 2009b).

1.1 INL High Temperature Electrolysis Laboratory

A photograph of the INL HTE laboratory dedicated to small-scale experiments with single cells and small stacks is shown in Figure 1-2.

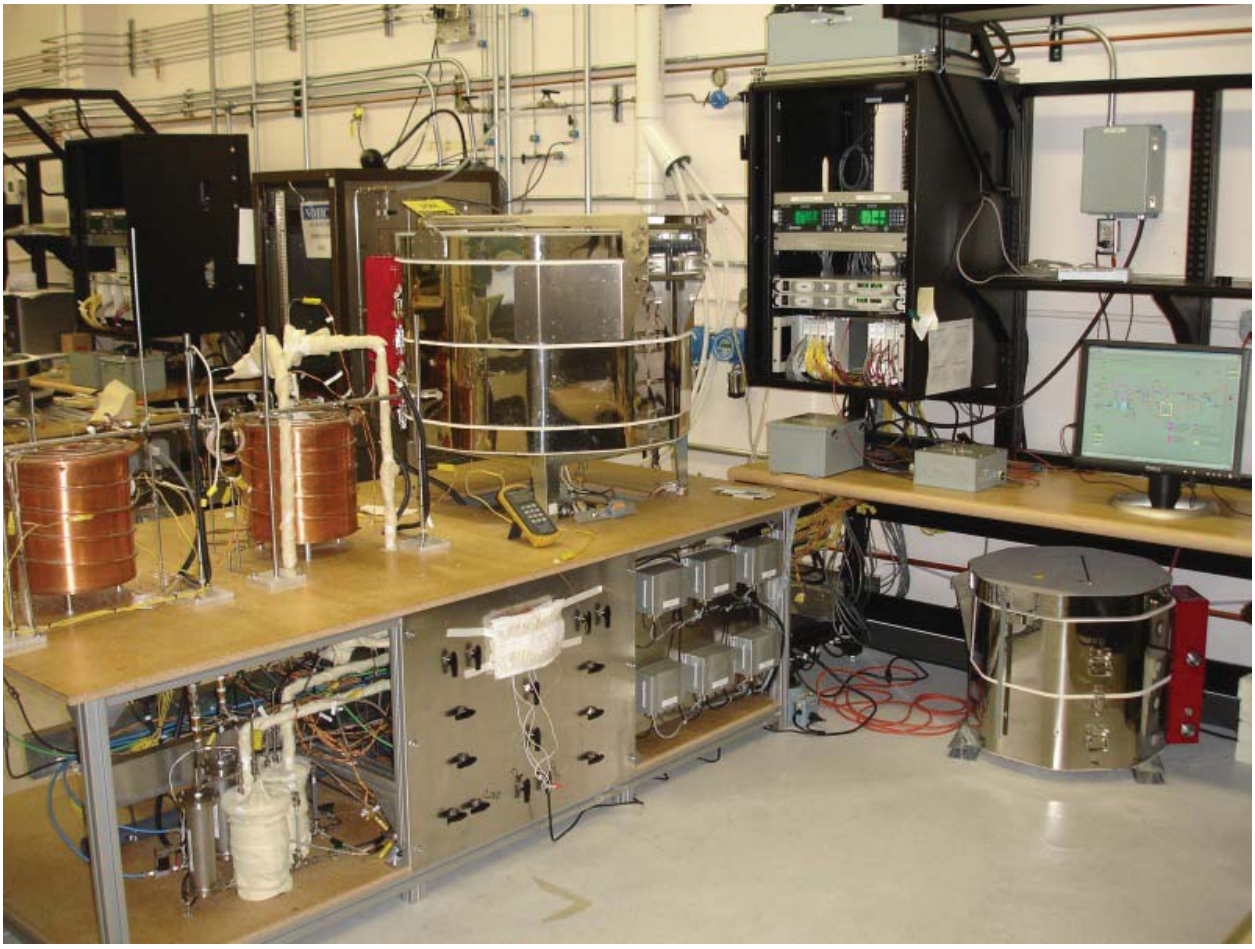

Figure 1-2. INL high-temperature electrolysis laboratory.

A comprehensive discussion of the INL high temperature solid oxide electrolysis bench-scale experiment is presented elsewhere (Stoots et al. 2009). This same facility is used for button cell testing as well as stack testing. A schematic of the test hardware found in Figure 1-2 is presented in Figure 1-3. Primary components include: gas supply cylinders, mass-flow controllers, a heated water-bath humidifier, on-line dewpoint sensors, temperature and pressure measurement instruments, high temperature furnace, and the solid oxide electrolysis cell. Nitrogen is used as an inert carrier gas. The use of a carrier gas allows for independent variation of both the partial pressures and the flow rates of the inlet steam and hydrogen while continuing to operate near atmospheric pressure. Inlet flow rates of nitrogen, hydrogen, and air are established by means of precision mass-flow controllers. Hydrogen is included in the inlet flow as a reducing gas in order to prevent oxidation of the Nickel cermet (**cer**amic-**met**al) electrode material. Air flow to the stack is supplied by the shop air system, after passing through a two-stage extractor/dryer unit. The cathode-side inlet gas mixture consisting of hydrogen and nitrogen is mixed with steam by means of a heated humidifier. The dewpoint temperature of the nitrogen-hydrogen-steam gas mixture exiting the humidifier is monitored continuously using a precision dewpoint sensor. All gas lines located downstream of the humidifier are heat-traced in order to prevent steam condensation.

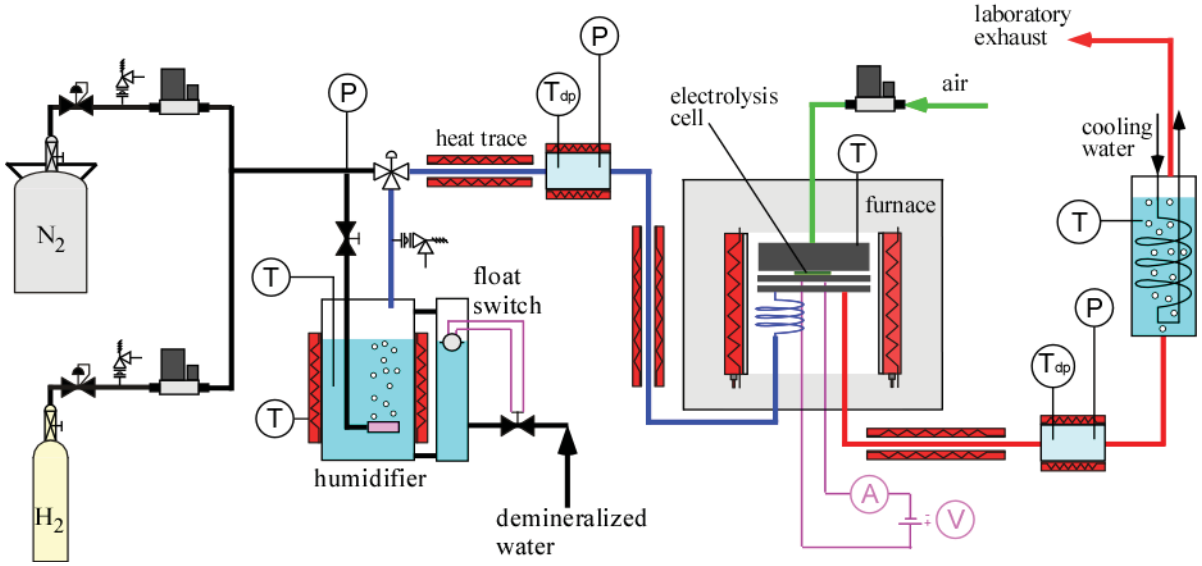

Figure 1-3. General schematic of one of INL solid oxide cell testing apparati.

Downstream of the mass-flow controllers, nitrogen is mixed with smaller flows of hydrogen gas. Hydrogen is included in the inlet flow as a reducing gas in order to prevent oxidation of the Nickel cermet electrode material. The nitrogen-hydrogen gas mixture is mixed with steam by means of a heated humidifier. The humidifier water temperature is maintained at a constant setpoint value using computerized feedback control. The dewpoint temperature of the nitrogen-hydrogen-steam gas mixture exiting the humidifier is monitored continuously using a precision dewpoint sensor. Pressure is also measured at the dewpoint measurement stations using absolute pressure transducers. Local stream pressure information is required to determine the mole fraction of steam in the gas mixture at the dew point measurement station. Since the nitrogen and hydrogen flow rates are fixed by the mass flow controllers, and the steam partial pressure is fixed by the bath temperature, the complete inlet gas composition is precisely known at all times. All gas lines located downstream of the humidifier are heat-traced in order to prevent steam condensation. Gas line temperatures are monitored by thermocouples and controlled by means of computer-controlled SCRs.

The electrolysis product stream exiting the furnace is directed towards a second dewpoint sensor and then to a condenser through a heat-traced line. The condenser removes most of the residual steam from the exhaust. The final exhaust stream is vented outside the laboratory through the roof. The rate of steam electrolysis is measured via two different, independent methods: (1) electrical current through the stack and (2) the measured change in inlet and outlet steam concentration as measured by the on-line dew-point sensors.

Herring et al. (2007) presented the progress of INL HTE research from small-scale bench testing to large-scale demonstration. INL has conducted experiments with following cells/stacks:

- Button cell testing (~1 W)
- Stack testing (200 W–5 kW)—electrode, electrolyte, and interconnect materials, flow channel materials and fabrication, inter-cell electrical contact, cell and manifold sealing issues, and cell durability.
- ILS testing (15 kW)—all previous issues plus multiple-stack thermal management, heat recuperation, feedstock heating, and hydrogen.

2. SOLID OXIDE CELL AND POLARIZATION LOSSES

This section provides a general introduction to solid oxide cell construction, material composition, and polarization (degradation) losses.

2.1 Solid Oxide Cell

A solid oxide cell is a key component of the electrolysis system. It consists of three main components: an electrolyte and two electrodes (Figure 2-1 and Figure 2-2). The electrolyte is a ceramic membrane that can conduct ions and is sandwiched between two porous electrodes that can conduct electrons: the steam/hydrogen electrode (commonly called anode in fuel cell mode) and the air/oxygen electrode (cathode in the fuel cell mode). In the fuel cell mode, oxygen molecules dissociate at the oxygen electrode and combine with electrons coming from an external electric power source to form oxygen ions (Figure 2-1b). The oxygen ions conducted through the electrolyte migrate towards the hydrogen electrode. The fuel (hydrogen or natural gas) is fed to the anode and reacts with the oxygen ions to form water and CO_2, while the resulting free electrons are transported via the external circuit through the load and back to the oxygen electrode. If the fuel cell is operated in the electrolysis mode (Figure 2-1a), the names and functions of the electrodes get reversed. Thus, the properties of the oxygen electrode should be such that it provides a component for oxygen gas to be easily reduced. Similarly, the function of the hydrogen electrode is to oxidize the fuel gas. The solid oxide electrolyte separates the reduction and oxidation reactions.

The most common materials in use for the solid oxide cells are listed in Table 2-1 (Gazzarri 2007). The electrolyte is a dense gas-tight ceramic layer, usually made from YSZ with a yttria content of 8 mol% to fully stabilize the electrolyte composition. The performance of the electrolyte depends on how well it can conduct oxide ions ($O^{=}$). The thinner the electrolyte, the higher its ionic conductance and the lower the cell's ohmic resistance. In an electrolyte-supported cell, the electrolyte thickness is large (150–250 μm), which leads to relatively high ionic resistance. Therefore, if the mechanical strength can be provided by the steam/H_2 electrode, the electrolyte thickness can be reduced by a factor of ~10.

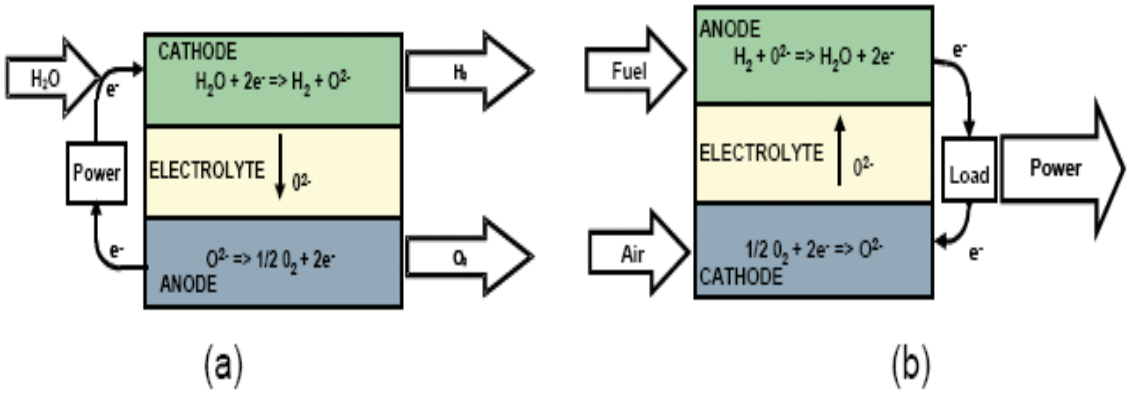

Figure 2-1. (a) Solid oxide electrolytic cell (SOEC); (b) solid oxide fuel cell (SOFC) (Guan et al. 2006).

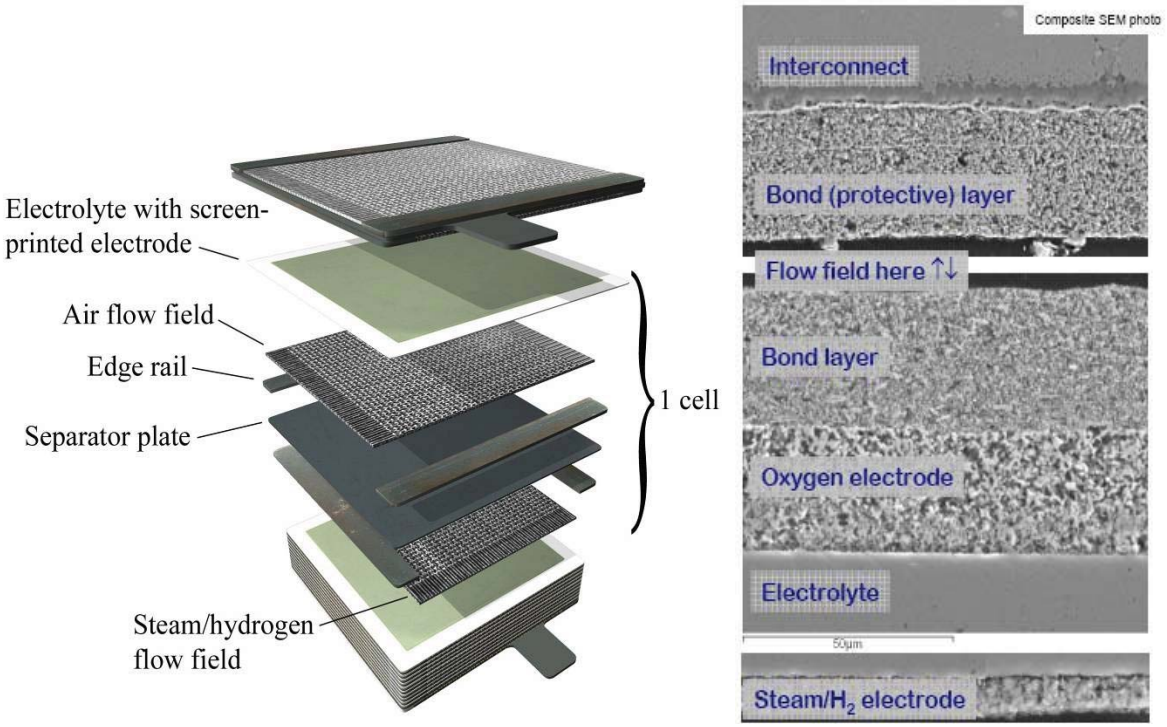

Figure 2-2. Ceramatec solid oxide cell/stack construction (scanning electron microscopy figure on the right is from Carter et al. 2008).

Table 2-1. Commonly used materials in SOFC/SOEC (Gazzarri 2007).

Component	Material	Acronym
Steam/hydrogen electrode	Ni - $Y_x Zr_{1-x} O_{2-x/2}$ (nickel-yttria stabilized zirconia)	Ni-YSZ
Electrolyte	$Y_x Zr_{1-x} O_{2-x/2}$ (yttria stabilized zirconia)	YSZ
Air/oxygen electrode	$Sr_xLa_{1-x} MnO_{3-\delta}$ + $Y_x Zr_{1-x} O_{2-x/2}$ (doped lanthanum manganite)	LSM-YSZ
Interconnect	Chromium-based alloys/ceramics or stainless steel	SS

The most common anode material for SOFC is a porous cermet made from Ni and YSZ. Electronically conductive, gas-tight interconnect plates connect the individual cells to form a stack. Since the electrolyte generally represents the highest resistivity layer in the cell, decreasing its thickness can lead to improved performance. The nickel cermet material (anode in the fuel cell mode, cathode in the electrolysis mode) has relatively high electronic conductivity and is therefore a logical choice for use as the mechanical support layer in electrode-supported cells. The ionic conductivity of ceramics is highly dependent on the ceramic temperature. Thus, high operating temperatures are required to obtain sufficient overall conductivity in the solid oxide cell. YSZ exhibits acceptable conductivity in the 700–1,100ºC temperature range, but if thermal cycling occurs, such as at start-up, the high operating temperature results in large thermal stresses in the cell components. Stresses can also be caused by large thermal gradients generated by the uneven distribution of electrochemical reaction sites. Finally, fabrication of the cell components also requires high temperatures that can cause detrimental residual stresses within the cell components. Guan et al. (2006) performed studies for reversible solid oxide cells, which were tested in both fuel cell and electrolysis modes. They selected YSZ (8 mol% Y_2O_3 doped zirconia) as electrolyte material. Selected oxygen electrodes were strontium-doped lanthanum manganite (LSM),

strontium-doped lanthanum ferrite (LSF), and lanthanum strontium cobalt iron oxide (LSCF). They used a samaria-doped ceria (SDC) interlayer for LSF and LSCF. LSCFs have increased ionic conductivity and may reduce the degradation rate in electrolysis mode. For the hydrogen electrode, Ni-YSZ was selected with a varying volume fraction of Ni (40–80%).

In the electrolyzer mode, the electrical energy is used to split hydrogen from steam. The electrolysis process is the reverse of the fuel cell process in which a mixture of steam and hydrogen is fed to the electrolytic cells. The oxygen migrates through the solid-state electrolyte as $O^{=}$ ions because of the imposed voltage. The cell voltage is about 0.4 V lower than that required in conventional electrolyzers because of the high operating temperature.

2.2 Polarization Losses

The polarization loss definitions described in this chapter are written strictly for a SOFC. Appropriate care should be applied when applying the same fundamentals for a SOEC case.

When a fuel cell is not connected to an external load, there is no current flow and the maximum reversible cell voltage or open circuit voltage can be calculated by the equilibrium Nernst potential for the specific electrochemical reaction system. The Nernst potential, V_{Nerst}, is calculated using the partial pressure of the chemical species at the cell inlet or outlet. However, it is more appropriate to calculate an average of the inlet and outlet values, V^{i}_{Nernst} and V^{o}_{Nernst}, where superscripts "i" and "o" represent inlet and outlet locations as

$$V_{Nernst} = \tfrac{1}{2}\left(V^{i}_{Nernst} + V^{o}_{Nernst}\right) \tag{1}$$

$$V^{i}_{Nernst} = -\frac{\Delta G^{0}}{n_e F} - \frac{RT}{n_e F}\ln\left(\frac{p^{i}_{H_2O}}{p^{i}_{H_2}\sqrt{p^{i}_{O_2}}}\right) \tag{2}$$

$$V^{o}_{Nernst} = -\frac{\Delta G^{0}}{n_e F} - \frac{RT}{n_e F}\ln\left(\frac{p^{o}_{H_2O}}{p^{o}_{H_2}\sqrt{p^{o}_{O_2}}}\right) \tag{3}$$

where

ΔG^{0} = change in Gibbs free energy at standard conditions and equals –RT ln[K(T)]

R = universal gas constant

T = cell temperature

K = equilibrium constant

n_e = number of electrons participating in the electrochemical reaction

F = Faraday's constant, and p is the partial pressure of respective species.

When a fuel cell starts supplying electric current to an external load, its operating voltage drops because of irreversibilities associated with internal resistances. The difference between the maximum reversible cell voltage or open circuit voltage (V_{OCV}) and the operating cell voltage (V_{open}) is termed polarization loss (η). Cell performance depends on the overall cell reaction and the type of reactants at the electrodes and the reaction product(s). Ivers-Tiffée and Virkar (2003) and Akkaya (2007) give a detailed

description of polarization losses. The total polarization loss of an operating cell consists of three dominant parts: activation (or charge transfer) polarization (η_{act}); concentration (or diffusion) polarization which includes chemical reaction polarization (η_{conc}); and ohmic resistance polarization (η_{ohm}).

$$\eta = \eta_{act} + \eta_{conc} + \eta_{ohm} \quad (4)$$

The current efficiency can be stated as the percent of current passing through an electrolytic cell (or electrode) that accomplishes the desired chemical reaction compared to the ideal case. For example, in the hydrogen fuel cell, ideally every hydrogen (H_2) molecule would react to produce two electrons that would contribute to the current flow. The inefficiencies arise from reactions other than the intended one taking place at the electrodes or the side reactions consuming the current. Some hydrogen, for instance, may go through the electrolyte and not react at all, or the hydrogen does react but the resulting current is driven through the electrolyte (not the electrode) and never contributes to the current flow.

The voltage efficiency is defined as the net voltage (cell equilibrium voltage minus the irreversible losses) divided by the maximum voltage. The irreversible voltage losses are attributed to polarization losses that primarily originate from three sources: activation, concentration, and ohmic polarizations.

Thus, the net cell voltage is the open circuit voltage minus the various polarization losses and can be written as:

$$V_{cell} = V_{open} - (V_{act} + V_{conc} + V_{ohm}) = V_{Nernst} - V_{loss} \quad (5)$$

Figure 2-3, developed by Windisch et al. (2002), shows the relative magnitude of various polarization losses in a SOFC. It shows that activation losses are the dominant mode of three types of polarization losses. It also shows the upper limit of current density for the fuel cell to operate.

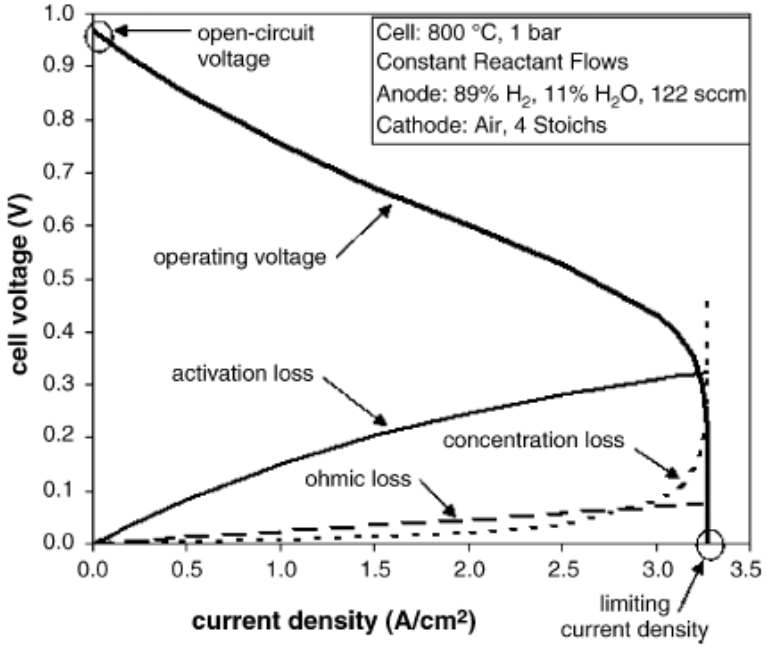

Figure 2-3. SOFC voltage-current characteristics for a single cell operating at 800°C (Windisch et al. 2002).

The overpotentials can be determined by the several models available in the literature—for example, Virkar (2007). However, the concentration overpotentials are different between the SOEC and SOFC modes because of the different gas transport mechanisms in the porous electrodes. Ni et al. (2006) showed that concentration overpotentials are the sole factor responsible for the different current-voltage (i-V) characteristics between the SOEC and SOFC modes. Their analytical model shows the differences in the gas transport mechanisms of the two modes. The selection of an electrode support can greatly affect the overall performance of a reversible solid oxide cell.

A hydrogen-electrode (fuel cell anode) support is favorable for the SOFC mode while an oxygen-electrode (electrolysis anode) support is favorable for the SOEC mode. Therefore, the details of both SOEC and SOFC operating conditions should be carefully considered in their design. If a specified solid oxide cell is mainly used for hydrogen generation, an oxygen-electrode (electrolysis anode) supported cell is recommended. Therefore, corresponding resistance of a SOFC is the cell resistance normalized by its area ($k\Omega \cdot cm^2$) and is called area-specific resistance (ASR). From the cell polarization and corresponding current density, an ASR can be defined as

$$ASR = (E - V)/i \tag{6}$$

where

E = either open circuit voltage potential (E_{OCV}) or the ideal Nernst potential (E_N), depending on whether one wants to (1) remove loss effects due to reactant leakage and variable reactant mixture supply and if one is focused on the cell material performance, or (2) focus on total cell performance (cell material and seals) (Gemmen et al. 2008).

Some methods for reducing this resistance include using:

- Electrodes with high electronic/ionic conductivity
- Appropriate bipolar plate/interconnect materials that are low in ohmic resistance and also complement the other cell component materials
- Thin, but structurally stable electrolyte with the ability to prevent shorting from one electrode to the other.

The important factor to remember about various polarization components is that they are not independent of each other. A change in partial pressure affects the concentration polarization, and it will also affect the activation polarization.

3. DEGRADATION PHENOMENA IN SOLID OXIDE ELECTROLYSIS CELLS

As INL progressively increases the scale of electrolyzer systems by increasing the number of solid oxide cells and stacks, it is important to understand and address the causes of performance degradation in SOEC stacks. Unfortunately, not many studies in the published literature address degradation and related issues in SOECs. Even for SOFCs, the issues of degradation, aging, and longevity are topics of ongoing research. As thinner electrolytes with higher ionic conductivity are developed, the overall cell polarization losses are dominated by the electrochemical losses at the anodes and cathodes. Even though the solid oxide cells have several differences while operating in power generating (fuel cell) and electrolysis modes, the degradation mechanisms in the two cases may have some similarities. Therefore, the knowledge of degradation mechanisms in SOFCs can be a starting point for the SOECs and can offer some guidance in identifying the research areas. This being the case, some known degradation background in SOFCs is reviewed here.

Ni et al. (2006) have developed models for concentration overpotential in SOECs and SOFCs, as shown in Figure 3-1(a) and (b), respectively. The cathode (hydrogen electrode) in the electrolysis mode is termed "anode" in the fuel cell mode. Similarly, the anode (oxygen electrode) in the electrolysis mode is termed "cathode" in the fuel cell mode.

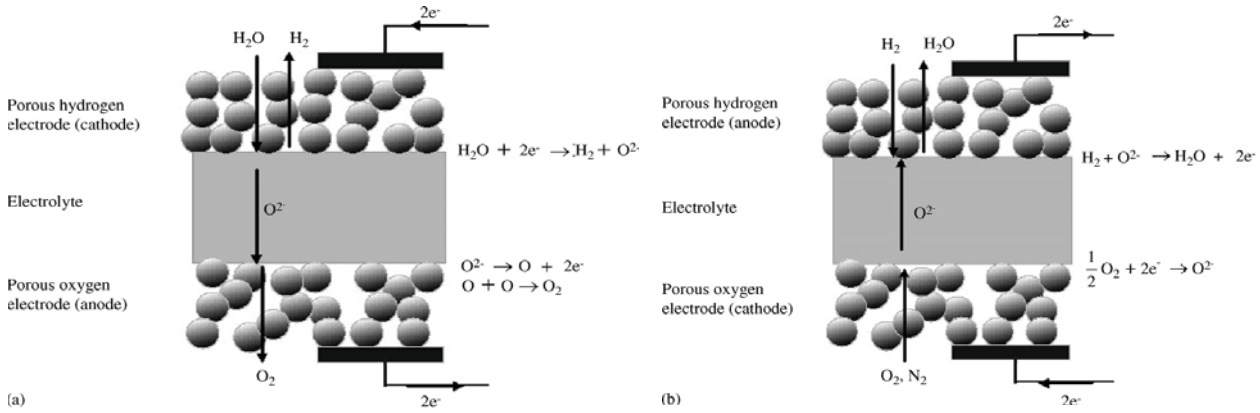

Figure 3-1. Operating mechanisms of solid oxide cells: (a) a SOEC in electrolysis mode, and (b) a SOFC in fuel cell mode (Ni et al. 2006).

3.1 Degradation Phenomena and Models

There are two common definitions for quantifying degradation given by Gemmen et al. (2008). The ASR represents an instantaneous performance measure. Another degradation definition is termed "average degradation rate," $D\overline{R}(t)$. It is defined for a time period of (t-t_0). Thus, for any cell voltage V(I_s, t), at a time t, average degradation rate, $D\overline{R}(t)$, is given by Gemmen et al. (2008) as

$$D\overline{R}(t) = \frac{V(i_s, t_0) - V(i_s, t)}{V(i_s, t_0) \times (t - t_0)} 100 . \quad (11)$$

ASR is best suited for comparing the performances of the same cell with two types of technologies, such as one type of interconnect design with another. However, DR is better suited to comparing cell performance with a stack performance of the same type of cells. To understand the degradation phenomena, a solid oxide electrolyzer needs to be operated and tested.

Figure 4-6 and Figure 4-7 show some of the data that were taken during the tests performed at INL. Current density, voltage, ASR, cell system temperature, reactants, and product flow rates are some of the commonly measured parameters during the tests. However, to understand the electrochemical behavior of the electrodes and electrolytes, their chemical microstructure has to be understood before and after an electrolysis operation. Also, the movement of impurities (for example, Ni, Cr) as a result of the electrolysis operation should be identified. The impact of the impurities' movement on electrochemical performance of a single cell and a stack should also be determined by making relevant measurements.

Recently, Virkar (2007) developed an overpotential model for a typical planar SOFC stack comprising several cells connected in series. He also gave the following argument in favor of developing a fundamental understanding of the degradation. In a stack, cell-to-cell characteristics should be as uniform as possible so that, at a given operating current, the voltage across each cell is essentially the same. If, because of some structural/fabrication flaws, the cells are not identical, the resistance and voltage drop will vary from cell to cell. In such a case, the remainder of the cells in the stack will drive the cell with higher resistance. In an extreme case, for the stack to continue operating, the voltage across a cell with higher resistance can even become negative, which can eventually lead to cell failure and increased local temperatures. This phenomenon can spread to adjacent cells in a domino effect.

However, interpretation solely based on visual observations, without a sound theoretical basis for all the phenomena occurring in a cell, may be misleading. In a cell, observations are the aftermath result of some other critical damage to the cell that has already taken place, so the visual observation alone may not be able to show the root cause of the problem. Some of the likely reasons of cell degradation include small initial compositional inhomogeneities resulting in large changes in properties, the formation of local hot spots leading to local changes in microstructures and material properties, electrode delamination due to thermal cycling/rapid heating, reaction between electrode and electrolyte forming a high-resistance layer, fuel and/or oxidant maldistribution, nonuniform oxidation of the interconnect, degradation of the seals, etc. In a normal SOFC, the direction of the (oxygen) ionic current is opposite to that of electronic current. However, if a cell has degraded to cause negative voltage, the direction of electron flow will reverse and both ionic and electronic currents will flow in the same direction.

Virkar (2007) developed a degradation model based on this premise; that is, a cell with higher resistance compared to the rest of the cells in the stack and operating under a negative voltage will be prone to degradation. Planar stacks are more likely to undergo such a degradation mechanism than tubular stacks. Therefore, the ability to measure voltage across each (planar) cell could help in preventing catastrophic failure by either performing preventive maintenance or shorting the bad cell. A similar degradation model of a SOEC can also offer some insight into the cell degradation phenomenon during the electrolysis mode.

According to Virkar (2007), one of the principal modes of failure of solid-state electrolytes is related to the generation of high chemical potentials and corresponding ultra-high pressure of neutral species within the electrolyte. For example, in an oxygen ion conducting solid electrolyte such as YSZ, under some thermodynamic conditions, oxygen chemical potential within the solid electrolyte, $\mu_{O_2}^{YSZ}$, may exceed the chemical potential of gaseous oxygen, that is, under certain conditions, $\mu_{O_2}^{YSZ} > \mu_{O_2}^{O_2\ electrode}$. The chemical potential of any reactant is a function of its partial pressure, $\mu_{O_2} = f(p_{O_2})$. Therefore, under certain conditions, $p_{O_2}^{YSZ} > p_{O_2}^{O_2\ electrode}$; and in some cases, $p_{O_2}^{YSZ} >>> p_{O_2}^{O_2\ electrode}$. If very high pressure develops, it may result in electrode delamination. This increases the cell resistance and then degradation propagates.

Under the same operating conditions of temperature and current density, a SOFC and a SOEC are likely to have the same ohmic and activation overpotentials. Over the past few years, extensive research has been performed relating to SOFC. Yet SOFCs have not reached their complete commercial success because of problems relating to their degradation, longevity, and cost. Some of the degradation mechanisms include contact problems between adjacent cell components, microstructural deterioration (coarsening) of the porous electrodes, and blocking of the reaction sites within the electrodes. Contact problems include delamination of an electrode from the electrolyte, growth of an electronically poorly conducting oxide layer between the metallic interconnect plates and the electrodes, and lack of contact between the interconnect and the electrode. Examples of microstructural degradation are oxygen electrode sintering, carbon deposition, and sulfur or chromium poisoning.

Delamination caused by thermal cycling increases ohmic resistance proportional to the delaminated area. The delaminated area also becomes inactive for electrochemical transport of ions across the electrode and the electrolyte. Chromium-based interconnect oxidation is another important mode that contributes to reducing electrical conductivity between the electrode and interconnect. Sometimes ceramic coatings are used to slow down the rate of oxidation and reduce the rate of chromia evaporation from the interconnects. It was also shown that the loss of performance resulting from interconnect detachment is less severe than that caused by electrode delamination because blocked transport of electrons can now easily move laterally in the electrodes as compared to ions being able to move within the electrolyte. The modeling exercise indicated that results of delamination are highly dependent on the inaccuracies in the knowledge of various cell parameters.

The severe temperature and electrochemical conditions in a solid oxide cell create the need for special materials and pose important challenges to the longevity of the different cell components. The requirements of a solid oxide cell are to facilitate chemical reactions and remove reaction products with the lowest possible resistance. Therefore, the density of reaction sites (sites per unit cell area) and transport paths in a cell should be maximized. For a solid oxide cell to be commercially viable, it should have a 40,000–50,000-hour lifetime. In order to facilitate such a long life, the degradation rate must be very low in all components of the cell stack. It is therefore important to have a fundamental understanding of the degradation mechanism for each component. During operation, any change in the cell that causes blocked reaction sites or transport paths for species will increase the overall cell resistance and thereby the degradation.

One important term used for describing reactions at both electrodes is the so-called triple-phase boundary (TPB). The TPB describes a site in the electrode where the electrochemical reaction takes place, shown as red dots in Figure 3-2 (Hauch 2007a). At the steam/H_2 electrode, this site is where all three phases (Ni, YSZ, and gas) are in contact with one other. Since the supply of oxygen ions in the YSZ, the supply of gas in the pores, and the means for transporting the electrons away in the Ni are simultaneously required, the electrochemical reactions are facilitated at the TPB. Therefore, in order to optimize the electrode performance, it is important to maximize the electrochemical activity at the TPBs. For a reaction to take place at the TPB, the gas stream must flow through the pores, Ni must be connected to the interconnect plate, and the YSZ must be connected to the electrolyte either directly or via YSZ in the electrode. Changes in the electrode-electrolyte interfaces and grain boundaries are highly influential in the degradation of the cell. These interfaces not only provide the TPB, but are also active for mass transfer, diffusion, and segregation of species involved in the fuel cell reactions during operation. Microstructural changes in the interfacial regions, such as impurity segregation, will also affect the cell's performance.

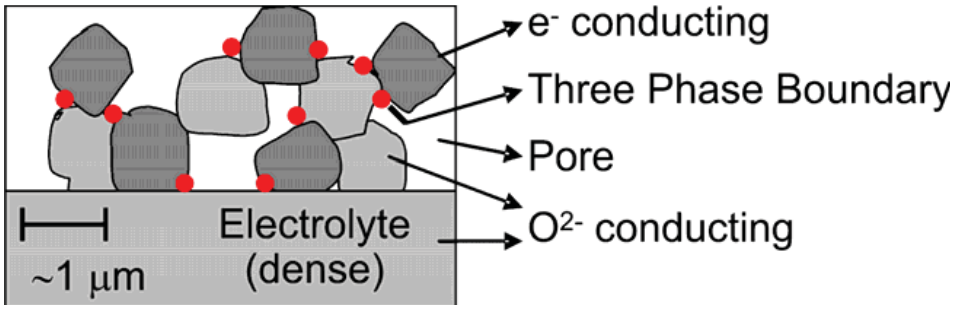

Figure 3-2. TPBs in a solid oxide cell, shown as red dots, where reactions take place (Hauch 2007a).

The problem of cell degradation also depends on the cell's operating conditions, such as operating temperature, because of increased atomic activity at higher temperatures. It has also been shown that the overall degradation in the cell voltage is more closely correlated to the polarization than to the current density. At high polarization and/or low temperatures (~750°C), the oxygen electrode (fuel cell cathode) degradation can be dominant. However, at low polarizations and/or higher temperatures, both electrodes contribute equally to the cell's degradation. From the impedance measurement, it is difficult to assign any degradation phenomenon responsible for overall cell degradation, which implies the importance of correlating electrical measurements with cell microstructural changes.

The mismatch in thermal expansion characteristics of the cell's different layers is a major cause of stresses during thermal cycling occurring during fabrication and operation. In addition, the nonequilibrium chemical reactions throughout the cell also generate large thermal gradients, which in turn generate thermal stresses. These thermomechanical phenomena cause the degradation of the contact between adjacent cell components, namely, the electrolyte-electrode and/or the interconnect-electrode interfaces. This degradation can lead to detachment of two adjacent layers, which results in reduced conductive paths available for electronic transport.

Another example of a degradation mechanism affecting SOFCs is the growth of an electrically insulating oxide layer between the interconnect plate and the electrodes, especially the fuel cell cathode. This leads to an increase in the cell ohmic resistance along the conductive path. The high temperature of operation promotes the kinetics of chromium oxide growth on the stainless steel interconnect plate. Extended periods of operation at high temperature and exposure to contaminants in the reactants also cause microstructural degradation. The electrochemical reactions in SOFCs are not restricted to the interface with the electrolyte, but take place within a few to tens of microns into the volume of the electrode. Therefore, a suitable electrode microstructure is of great importance in providing active surface area at the TPB for electrochemical reaction and sufficient porosity for gas species transport. Consequently, degradation mechanisms that affect electrode microstructure can compromise the cell's performance, stability, and durability.

4. PERFORMANCE OF SINGLE ELECTRODE-SUPPORTED CELLS IN THE ELECTROLYSIS MODE

This chapter describes the performance of single electrode-supported cells operating in the electrolysis mode. In the fuel-cell mode of operation, anode-supported cells represent the state-of-the-art in terms of performance. In an anode-supported SOFC, the anode is typically 1–1.5 mm in thickness while the electrolyte thickness can be as low as 10 μm. In the electrolysis mode, it may be preferable to use an oxygen-electrode-supported cell. A detailed overview of the apparatus that was developed for testing single electrode-supported cells in the electrolysis mode is described is described in this section, and preliminary test results are provided.

4.1 Single-Cell Test Apparatus Design and Fabrication

The test fixture and test stand was designed to evaluate the performance of individual cells without the complicating effects of interconnects. A modified version of this test fixture could be used to test individual cells plus interconnects.

Referring to the exploded view provided in Figure 4-1, a steam hydrogen mixture enters through a 1/4-in inconel coiled tube into the inlet hole in the bottom of the Hastelloy-X (HastX) base plate. It then flows through a diverging flow channel milled into the HastX base plate and passes through a slot in the bottom of the alumina cell holder. The slots can be seen in Figure 4-2. An alumina felt gasket is used to seal the HastX base plate against the alumina cell holder. The flow then passes under the cell through a corrugated/perforated nickel flow channel (flow field). The flow field establishes the gap for the steam-hydrogen flow channel under the cell while also serving as an electrical conductor. A 0.010-in nickel foil underneath the flow channel serves as a current collector. The Ni foil, flow channel, and mesh are sized to fit into the inner square recess machined into the alumina cell holder. The cell holder and air flow distributor material is fabricated from alumina in order to minimize the potential for chromium poisoning of the cell electrodes. The cell holder was machined in the bisque state and then fired. During firing, the bisque alumina shrinks by about 15%. This shrinkage must be taken into account when doing the machining such that the desired dimensions are achieved in the final dense alumina part.

Electrical contact with the electrodes is accomplished using a gold mesh on the air-side and a nickel mesh on the steam-hydrogen side. A gold wire in direct contact with the nickel foil serves as the steam-hydrogen side power lead and voltage tap. The wire just fits in one of the grooves of the flow channel. The two ends of this wire are fed out through the two small holes shown in the bottom of the alumina cell holder, visible in Figure 4-2(a). After passing along the bottom of the cell, the steam-hydrogen flow exits the alumina cell holder through a second slot and flows through a converging passage in the HastX base plate and out through an 3/8-in OD inconel outlet tube. The outlet tube is sized larger than the inlet tube in order to minimize back pressure on the cell seals to prevent leakage. The steam/hydrogen flow field is a corrugated/perforated nickel foil.

The cell is placed on a shelf milled into the alumina cell holder just above and in contact with the Ni mesh (Figure 4-2(b)). The cell dimensions are 50 × 50 × 1.5 mm (thickness). A nickel paste was used to enhance electrical contact between the cell and the nickel mesh, flow field, and foil. To help with sealing, an alumina felt gasket is placed on the shelf underneath the cell and an alumina-based ceramic paste (Aremco Products, Ceramabond 552) is distributed around the top outer edge of the cell to seal the gap between the cell and the alumina cell holder.

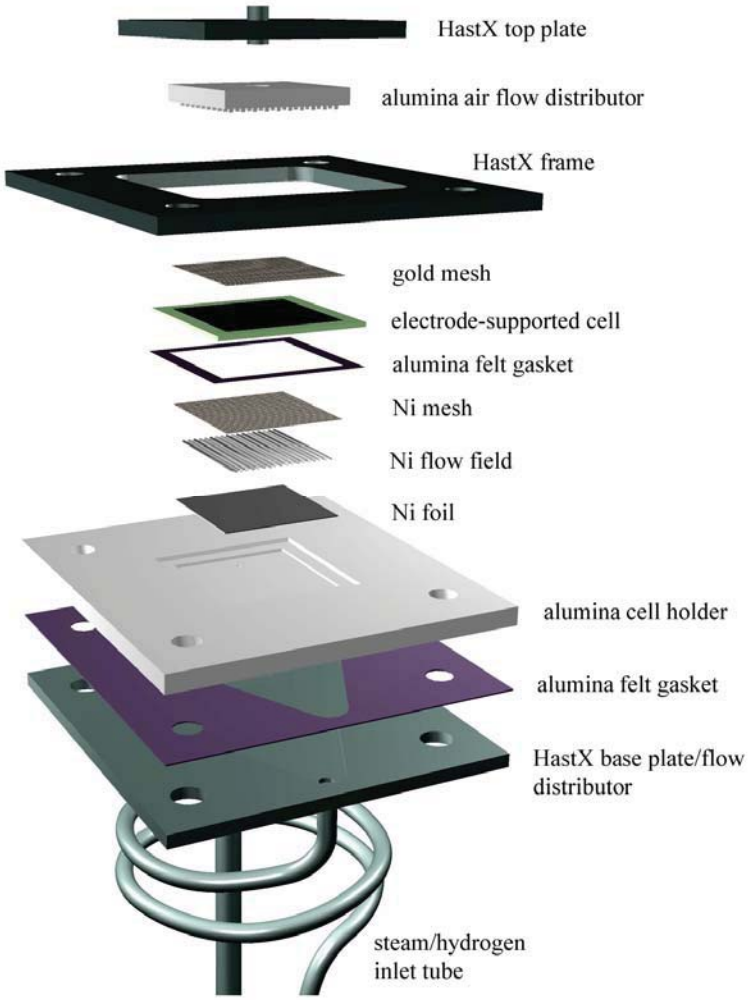

Figure 4-1. Exploded view of cell test fixture.

Figure 4-2. (a) alumina cell holder; (b) cell holder with cell in place.

A gold mesh contacts the oxygen electrode on the oxygen side of the cell. This gold mesh is held against the oxygen electrode by the alumina air flow distributor. The air flow distributor has an array of square protuberances milled into its surface (Figure 4-3), creating a gap for air flow while also compressing the gold mesh against the air-side electrode. A gold wire is positioned in one of the grooves, in contact with the gold mesh, for current collection. One end of this wire is used as a power lead and the other end is used as a voltage tap.

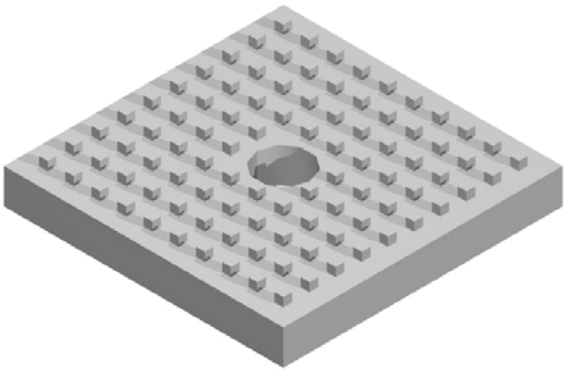

Figure 4-3. Alumina air flow distributor.

Air is introduced to the top side of the cell through an inlet tube welded to the HastX top plate. This tube protrudes slightly into a central hole in the alumina air flow distributor. A seal was formed between the HastX top plate and the alumina air flow distributor by means of an alumina felt gasket and a ceramic paste. After exiting the central hole in the air flow distributor, the air impinges on the cathode side of the cell and flows radially outward through the array of protuberances. The air then exits into the furnace volume.

A fixed compressive load is applied to the entire cell stack between the alumina cell holder and the HastX top plate by means of weights, as shown in the test stand overview diagram (Figure 4-4). This load simultaneously compresses the cell against the nickel mesh, flow channel (flow field) and foil on the bottom steam/hydrogen side of the cell and against the gold mesh on the air/oxygen side. It also compresses the cell against the seal around the outer edge of the cell, which rests on the shelf milled into the alumina cell holder. The HastX weight plates are held in alignment by the upper portion of the threaded rods which extend upward for this purpose.

A fixed compressive load is independently applied between the HastX frame, the alumina cell holder, and the HastX base plate. This load is generated by the compression of four springs located under the test stand base support outside of the furnace. The springs will be compressed a fixed amount that is determined by the height of the spool pieces by tightening a nut on the threaded rods. The threaded rods are fed through the alumina spacer tubes. These spacer tubes determine the height of the cell holder inside the furnace. The spring-generated load is intended to compress the seal between the cell holder and the base plate. This seal was formed by alumina felt impregnated with alumina slurry. A nut is visible on the threaded rods in Figure 4-4 just above the HastX frame and below the weight plates. This nut represents the upper stop for this compressive load. The extension of the threaded rods above the nuts is for the purpose of aligning the weight plates. Note that the weight plates are floating above these nuts since they are resting on the HastX top plate.

A photograph of the test stand installed in the furnace base is provided in Figure 4-5. Note that the base support is located outside of the furnace. Holes were drilled in the bottom of the kiln for pass-through of the flow tubes, alumina spacer rods, power leads, and instrumentation.

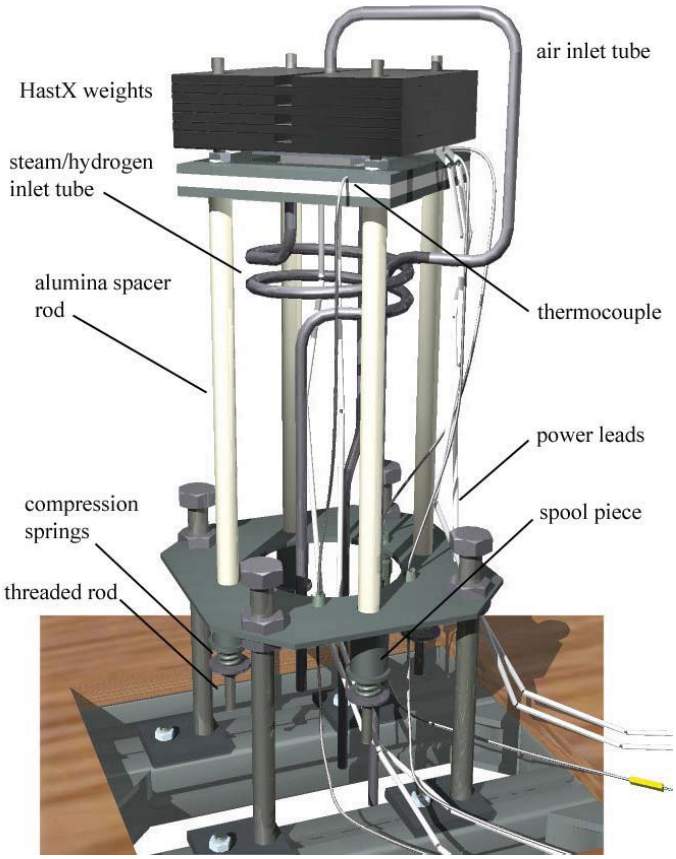

Figure 4-4. Test stand overview.

Figure 4-5. Test stand installed in furnace base.

4.2 Cell Reduction

The electrode-supported cells tested in this study are supported by the porous 1.5 mm thick steam-hydrogen electrode whose initial composition is nickel oxide and YSZ. The nickel oxide must be reduced to nickel metal in order for the electrode to become electronically conductive. This reduction process is accomplished by exposing the electrode to increasing levels of hydrogen gas at 900°C, as indicated in Table 4-1. The initial heatup of the cell (step 0) is performed under inert gas at a heatup rate of 1°C/min to 900°C. The cell is then exposed to varying nitrogen-hydrogen-steam gas mixtures for the time durations indicated in the table. The steam was introduced by bubbling the nitrogen-hydrogen gas mixture through a room-temperature water bath (humidifier). The corresponding steam flow rates can be calculated based on the nitrogen and hydrogen flow rates and the bath temperature. These calculated steam flow rate values are listed in the table. The steam/hydrogen electrode of the reduced cell is silver/gray in color.

Table 4-1. Cell electrode reduction procedure.

step	Hold time (min)	H_2 Flow rate (sccm)	T_{dp} (°C)	H_2O flow rate (sccm)	N_2 flow rate (sccm)	Air flow rate (sccm)	T_{cell} (°C)	y_{H2O}
0 (heatup)	n/a	0	bypass	0	500	500	1°C/min	0
1	75	80	bypass	0	500	580	900	0
2	7.5	160	bypass	0	500	660	900	0
3	7.5	160	22	20.8	500	660	900	0.031
4	5	320	22	25.9	500	820	900	0.031
5	5	500	22	23.7	250	750	900	0.031
6	5	500	22	15.8	0	500	900	0.031

4.3 Test Procedure and Analysis

This section describes how test conditions are to be determined. The nominal active area for the cells in this study is 16 cm^2. The maximum current density is usually set such that the maximum cell voltage is near the thermal neutral voltage (V_{tn} = 1.287 V at 800°C). Once the current density and cell area are known, the total cell current is known ($I = i \times A_{cell}$) and the molar hydrogen production rate can be determined directly from Faraday's law:

$$Q_{M,H_2,prod} = \frac{I}{2F}. \tag{12}$$

This molar value can be converted to a standard volumetric flow rate (e.g., sccm) by dividing it by the standard-state molar density, ρ_M = 44.615 mol/m^3.

A desired value for maximum fraction of steam utilization can then be specified. Depending on the objective of the test, this value could range from 0.2–0.9. Low values of steam utilization generally yield better cell performance in the electrolysis mode. High values can cause localized steam starvation and result in lower cell performance. Analysis of large-scale systems has indicated that overall system performance drops off for steam utilization values below ~0.5, but is fairly flat above that value (O'Brien et al. 2009b). Once the desired steam utilization is specified, the required inlet steam flow rate can be determined from

$$Q_{H_2O,i} = \frac{Q_{H_2,prod}}{U_{H_2O}} \tag{13}$$

Because steam is introduced (in this case) using a humidifier, the steam flow rate depends on both the inlet dew-point temperature, which is approximately the same as the humidifier bath temperature, and the flow rates of nitrogen and hydrogen. So the inlet dew-point temperature must be specified. We typically use a value of 50–70°C for single-cell testing.

For testing in the electrolysis mode, a reasonably high inlet dew-point temperature is required, typically 60–70°C. Once the inlet dew-point temperature is specified, the corresponding inlet mole fraction of steam is given by

$$y_{H_2O,i} = \frac{P_{sat}(T_{dpi})}{P_T} \tag{14}$$

where

$P_{sat}(T_{dpi})$ = the vapor pressure of steam at the specified inlet dew-point temperature, obtained from an appropriate correlation such as the Antoine equation. The total required gas flow of nitrogen plus hydrogen can then be obtained from

$$Q_{gas,i} = Q_{H_2O,i} \frac{1 - y_{H_2O,i}}{y_{H_2O,i}} \tag{15}$$

The inlet flow rate of hydrogen can be determined by specifying the desired inlet mole fraction of hydrogen, typically 0.1–0.2. Inlet hydrogen is required to maintain reducing conditions on the nickel cermet material. The respective flow rates of hydrogen and nitrogen are then obtained from

$$Q_{H_2,i} = \frac{y_{H_2,i}}{y_{H_2O,i}} Q_{H_2O,i} \text{ and} \tag{16}$$

$$Q_{N_2} = Q_{gas} - Q_{H_2,i} \tag{17}$$

Air is typically used on the oxygen side of the cell as a sweep gas in order to prevent buildup of pure oxygen. The flow rate of air is scaled with respect to the oxygen production rate,

$$Q_{O_2,prod} = Q_{H_2,prod} / 2 \tag{18}$$

as follows:

$$Q_{air} = \frac{N_{O_2 prod} Q_{O_2,prod}}{y_{O_2,air}} \tag{19}$$

where

N_{O2prod} = a factor indicating the number of oxygen production equivalents desired in the sweep air and y_{O2}, air is the mole fraction of oxygen in the sweep gas ($y_{O2,\ air}$ = 0.21). Typically, N_{O2prod} = 1, which yields an outlet sweep gas mole fraction of oxygen equal to 0.347.

Once the cell operating temperature is selected (typically 800°C), the test conditions are fully specified.

4.4 Preliminary Test Results

The first indication of cell performance that can be observed is the open-cell potential, which can be calculated using the Nernst equation as given in Equations (2) and (3): Generally, for single-cell testing, if the observed open-cell potential is different from the theoretical value by more than a few millivolts, it points to a possible problem with the cell such as gas leakage, a cracked cell, or a short circuit. Open-cell potentials observed for the cells tested in this study were all within 2 mV of the theoretical value given by Equation (20).

Initial electrolysis performance of these cells was evaluated by acquiring data for voltage-current polarization curves at three different operating temperatures. These polarization curves are presented in Figure 4-6 as cell voltage versus current density. The inlet gas flow rates and dewpoint temperature used during these sweeps are indicated in the figure. The sweeps were performed by varying the applied cell operating voltage from a value just below the open-cell voltage to a value of 1.3 V, which is just above the thermal neutral voltage. Current densities at 1.3 V were 0.456, 0.553, and 0.613 A/cm^2 at 800, 850, and 900°C, respectively. Negative values of current density in Figure 4-6 correspond to the fuel cell mode of operation and positive values represent the electrolysis mode. The polarization curves are linear through the zero-current transition from fuel-cell mode to electrolysis mode, indicating that activation does not contribute significantly to the observed overpotentials. Cell voltage increases nearly linearly at low current density, but at an increasingly higher rate at higher current densities. The nonlinear behavior at high current density is due to concentration overpotential associated with steam consumption.

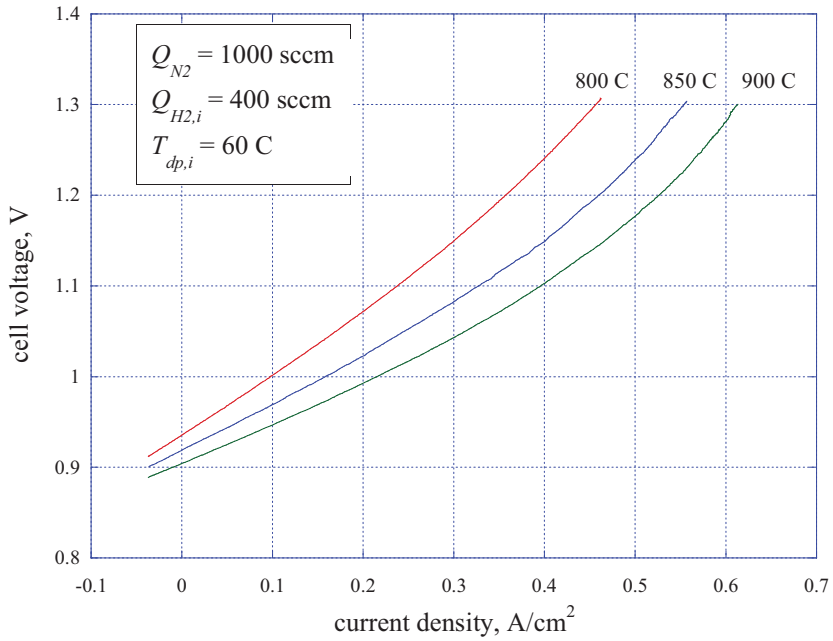

Figure 4-6. Polarization curves for electrode-supported cell.

Area-specific resistance (ASR) values for this cell are plotted in Figure 4-7 as a function of current density. These "apparent" ASR values are defined by (similar to that defined in Equation (6))

$$ASR = \frac{V_{cell} - V_{OC}}{i}. \qquad (21)$$

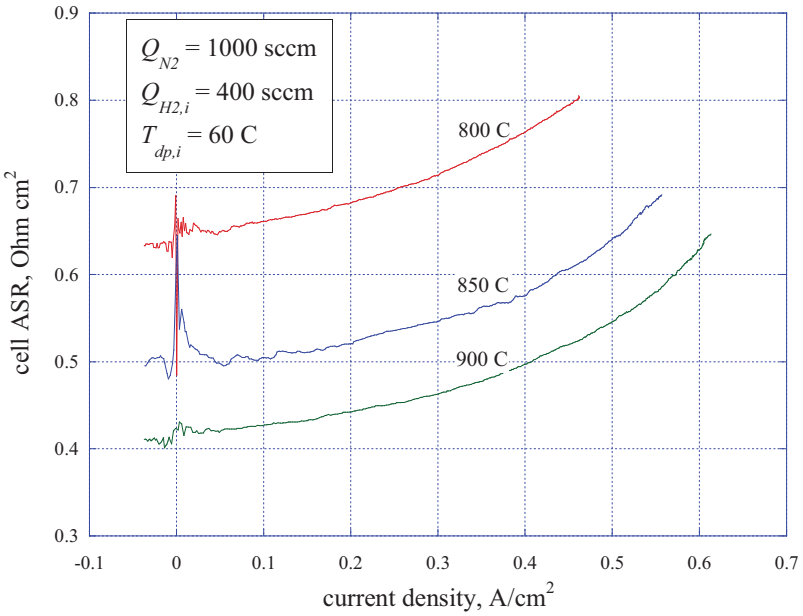

Figure 4-7. Area-specific resistance for electrode-supported cells as a function of current density.

Low-current-density ASR values are approximately 0.65, 0.50, and 0.42 Ohm·cm^2 at 800, 850, and 900°C, respectively. The apparent ASR values increase significantly with current density, again reflecting the effect of steam consumption.

Reduction of the steam-hydrogen nickel cermet electrode is accomplished by exposing the electrode to increasing levels of hydrogen gas at 900°C. A detailed methodology for determining gas flow rates for cell testing has been provided. Initial electrolysis performance of these cells was evaluated by acquiring voltage-current polarization curves at three different operating temperatures over a voltage range from a value just below the open-cell voltage to a value of 1.3 V. Low-current-density ASR values were approximately 0.65, 0.50, and 0.42 Ohm·cm^2 at 800, 850, and 900°C, respectively. The apparent ASR values increase significantly with current density, reflecting the effect of steam consumption.

4.5 Initial and Long-Term Performance of St. Gobain Electrode-Supported Cells

Initial performance of St. Gobain cell 316-03 was characterized by performing several DC potential sweeps. Results of these sweeps are presented in Figure 4-8 and Figure 4-9. The initial sweeps were performed at 800, 850, and 900°C with humidifier bath temperatures of 60 and 70°C. Each figure shows both a series the *V-i* polarization curves and a series of *ASR-i* curves. The voltage-current density curves are nonlinear, curving upward at high values of current density, revealing the effects of steam starvation and mass transfer through the thick (1.5 mm) steam-side electrode. This effect is more noticeable in the lower dewpoint data of Figure 4-8 than in Figure 4-9.

Cell area-specific resistance values decrease with increasing operating temperature and increasing steam content. The apparent ASR values presented in Figure 4-8 than in Figure 4-9 are calculated from Eqn (21). Initial low-current *ASR* values for the 60°C inlet dewpoint sweeps were 0.62, 0.52, and 0.48 Ohm·cm^2 at 800, 850, and 900°C, respectively. Corresponding values for the 70°C inlet dewpoint sweeps were 0.57, 0.48, and 0.41 Ohm·cm^2. These initial ASR values are quite good, as low as have been observed with the highest performing electrolyte-supported button cells tested at INL.

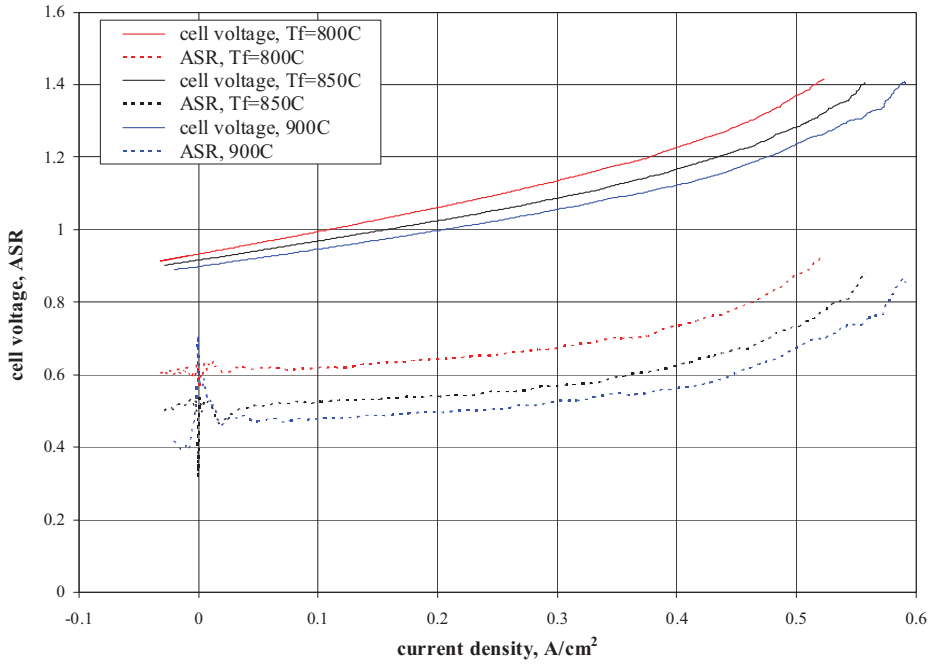

Figure 4-8 Cell voltage and ASR as a function of current density and operating temperature, initial sweeps, T_{dpi} = 60°C.

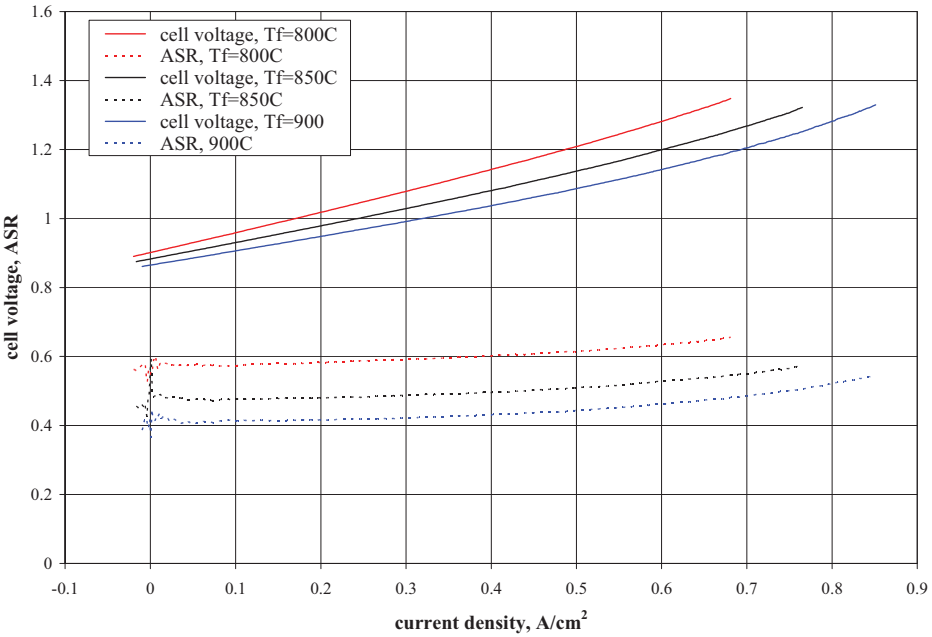

Figure 4-9 Cell voltage and ASR as a function of current density and operating temperature, initial sweeps, T_{dpi} = 70°C.

Hydrogen production rates during cell operation can be calculated based on cell current using Faraday's law. In addition, hydrogen production rates can be determined independently based on inlet and outlet dewpoint measurements. These measurements provide a direct indication of steam consumption rate, which on a molar basis is equal to the hydrogen production rate. Representative plots of inlet and outlet dewpoint temperatures and hydrogen production rates measured during a sweep are presented in Figure 4-10. In this figure, the inlet dewpoint temperature is essentially constant, as

expected, with a value of 67.2°C. The outlet dewpoint temperature decreases with increasing cell current, due to conversion of steam to hydrogen. Hydrogen production rates are also presented in the figure in standard cubic centimeters per minute (sccm). The straight black line represents the hydrogen production rate based on cell current, using Faraday's law. The green line represents the hydrogen production rate base on the inlet and outlet dewpoint temperatures. This line naturally includes some scatter, but the agreement between the two independent measurements of hydrogen production rates is generally quite good, providing confidence in the experimental results.

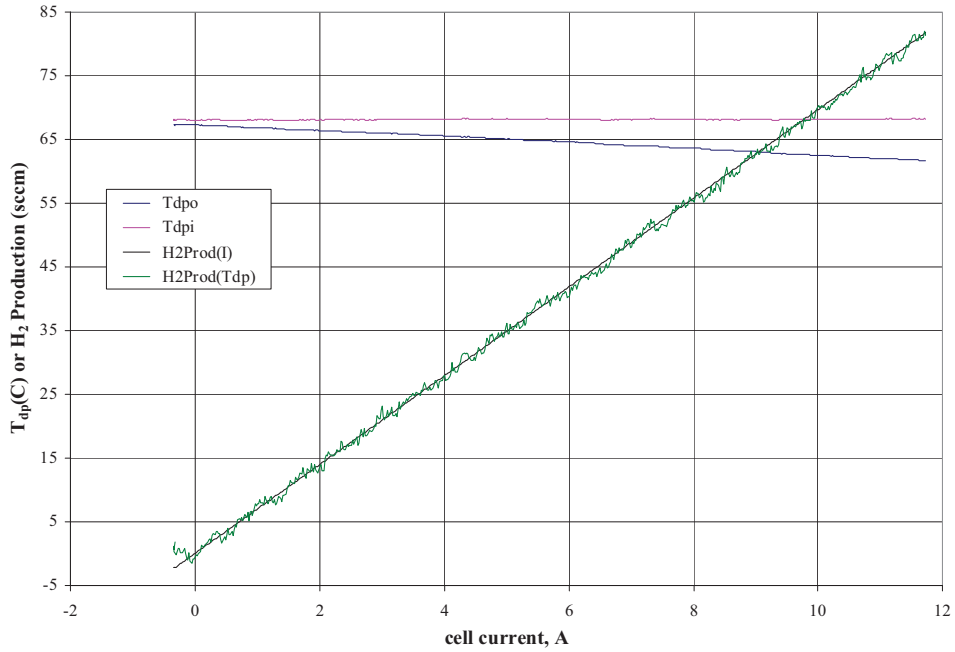

Figure 4-10 Dewpoint temperatures and hydrogen production rates as a function of cell current, T_f = 850°C, T_{dpi} = 68°C.

Long-term operation of this cell was initiated on July 17, 2009. This cell was subsequently operated for over 600 hours at 850°C. During the first 250 hrs. of operation, the cell was operated at a voltage of 1.21 V, with a nominal inlet dewpoint value of 60°C. At this time, a series of sweeps was performed for comparison to the initial sweeps. These sweeps were performed at both 60 and 70°C inlet dewpoint temperatures. Subsequently, the long-term durability test was continued, retaining the higher inlet dewpoint value of 70°C. At an elapsed time of 590 hrs, a final sweep was performed.

Results of long-term durability testing for this cell are presented in Figure 4-11 through Figure 4-13. Figure 4-11 shows the time history of cell voltage and current over 590 hours of elapsed test time. There is a step change in voltage and current at ~260 hours, associated with an increase in the humidifier bath temperature from 60 to 70°C. This change in inlet steam content yielded a lower cell ASR value, resulting in a lower open-cell voltage, and a higher cell current at the same operating voltage.

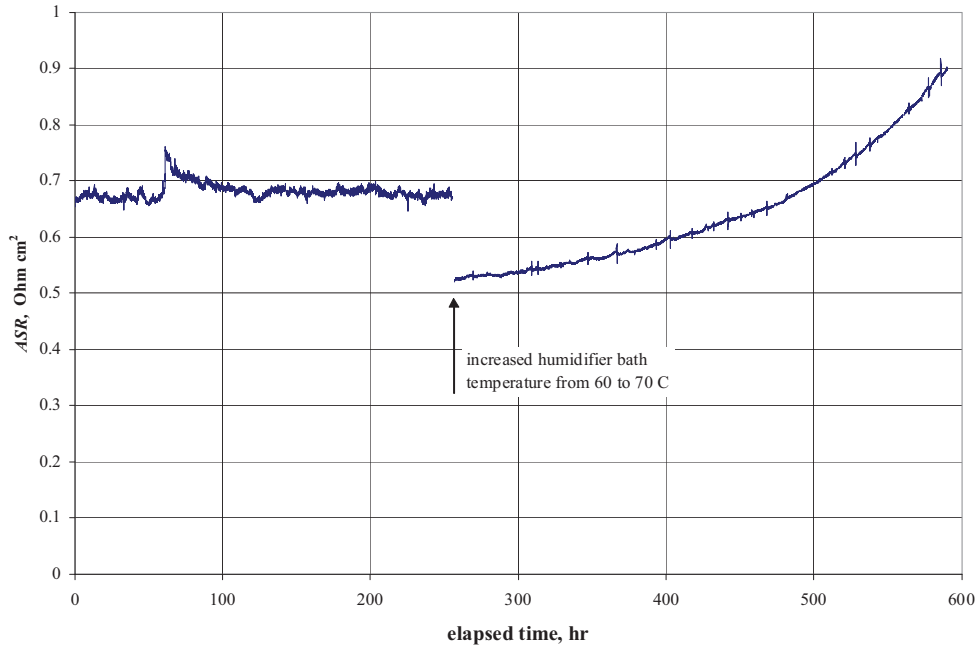

Figure 4-11 Cell area-specific resistance, long-term durability test.

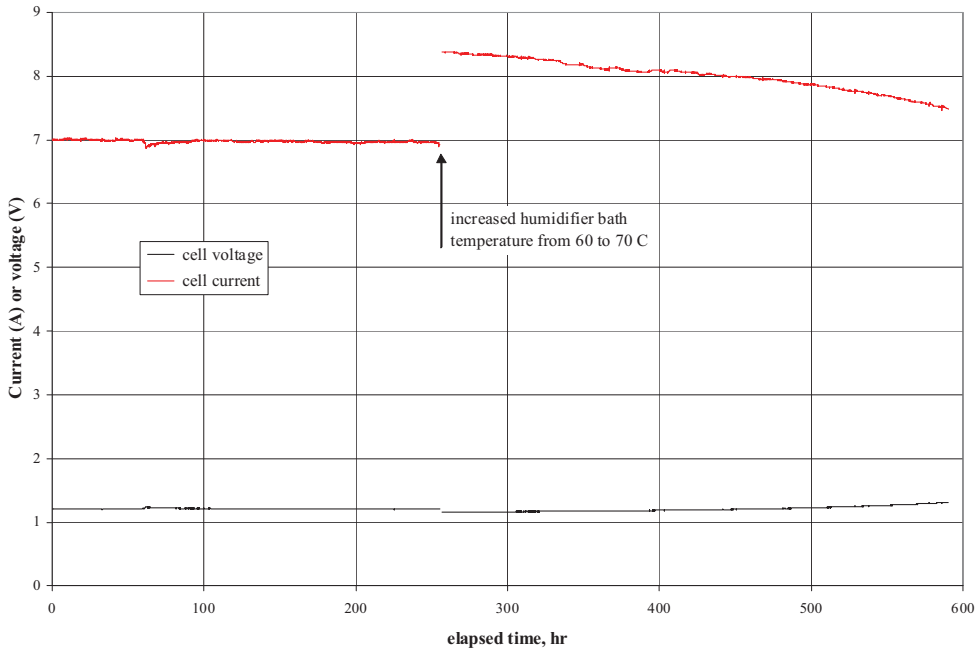

Figure 4-12. Cell voltage and current, long-term durability test.

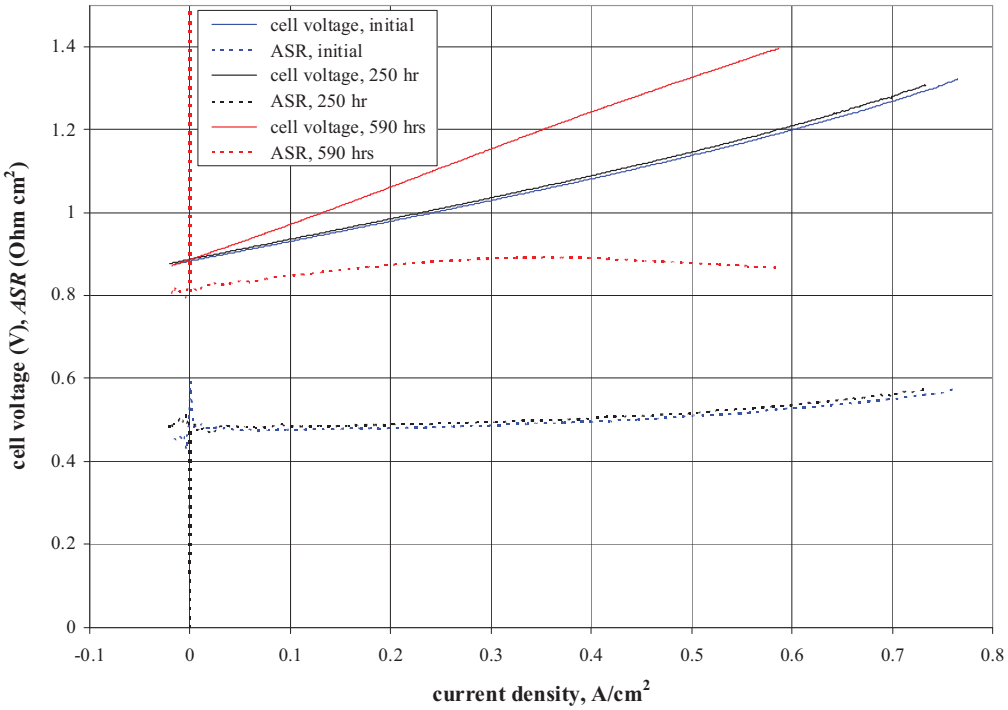

Figure 4-13. Cell voltage and ASR as a function of current density and cell operation time, T_{dpi} = 70°C.

Cell voltage and current were very stable for the first 250 hrs of operation, indicating essentially zero performance degradation over that time period. However, after performing two sweeps at this time and increasing the bath temperature, performance degradation began to occur. This degradation is more evident in the plot of cell *ASR* presented in Figure 4-12. For the first 250 hours of operation, the cell *ASR* at the fixed operating condition of V_{cell} = 1.21 V was nearly constant at ~0.67 Ohm cm^2. After increasing the bath temperature, the *ASR* value immediately decreased to ~0.52 Ohm cm^2, as discussed previously in conjunction with the sweeps. Thereafter, the ASR value begins to increase, attaining a value of 0.90 Ohm cm^2 at 590 hrs. More durability testing with this type of cell will be required to determine the exact cause of the accelerated degradation that was observed with this cell after 250 hours. The most obvious culprit is the increased steam content, but the cell current also increased significantly and two sweeps were performed at 250 hours.

A final sweep was performed at 590 hrs. Figure 4-13 presents cell voltage and *ASR* values as a function of current density for three sweeps with the humidifier bath at 70°C. Cell voltage and ASR values for the initial sweep and the 250-hr sweep are nearly identical. However, for the 590-hr sweep, cell voltage increases much more rapidly with current density. In addition, the ASR values are much higher at 590 hrs. The plot of *ASR* versus current density at 590 hrs has a different shape than for the earlier times. This difference in shape is at least partially due to the fact that the cell voltage for this sweep exceeded the thermal neutral voltage of 1.29 V. Beyond the thermal neutral voltage, the cell begins to heat up, which results in a lower *ASR* value.

5. PERFORMANCE OF THE NASA BI-ELECTRODE SUPPORTED CELL

5.1 Button Cell Fabrication by NASA

The NASA cell, a bi-electrode supported cell or BSC, is structurally symmetrical with both electrodes supporting the thin electrolyte and containing micro-channels for gas diffusion. The electrodes are made by freeze-casting—a modified tape casting technique that creates the many micro-channels in the YSZ electrode green tape. In freeze-tape casting, an aqueous or organic slip is cast across a freezing bed and micron size ice crystals start to form at the Mylar side of the tape. The microcrystals increase in size and form continuous ice crystals that grow larger towards the top, creating a natural gradient in porosity in the green tape; the green tape is placed in a freeze dryer and the ice crystals are removed by sublimation in a vacuum, leaving the micro-channels behind for gas flow. Symmetrical cells are fabricated by taking two green parts cut from the same piece of green freeze-cast tape, depositing a thin electrolyte layer between the tapes, and laminating the tapes together with the small pores facing each other, forming the YSZ tri-layer as shown in Figure 5-1. Cells with 2.54 cm O.D. were prepared by firing the YSZ tri-layers at high temperature, followed by infiltration of the electrodes. Ni-nitrate was used for the SOFC anode and stoichiometric solutions of nitrates for the LSF cathode. Cells were allowed to dry/solidify prior to heat treatment for decomposition of the nitrates into metals or metal oxides depending on the electrode. This infiltration procedure was performed multiple times on both the anode and cathode to achieve suitable electrodes. The cells were then bonded to the bottom end of a 1 in. O.D. YSZ tube using a high temperature glass ceramic (Figure 5-2).

A platinum wire was placed on both sides of the cell to measure the voltage and then Ni-mesh was used on the H_2 electrode and Ag mesh on the air electrode as current collectors; Au ink was used to attach the platinum wires and the other leads to the cell.

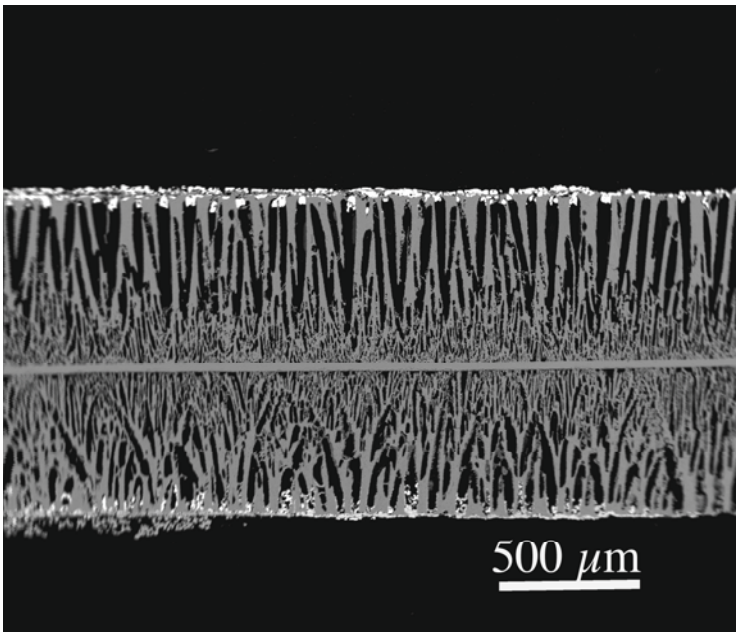

Figure 5-1. Cross section of a sintered BSC cell showing the thin YSZ (white) electrolyte in the center and the YSZ scaffolds, and the micro channels (black) formed by the ice crystals during freeze-casting, and then removed during freeze drying. The bright white at the top and bottom of the cell is Au ink.

Figure 5-2. NASA button cell mounted on support YSZ tube.

5.2 Button Cell Test Results

During testing, the tube is suspended in one of the smaller furnaces. The active cell area is approximately 2.25 cm^2. A type-K stainless-steel sheathed thermocouple is mounted on the tube and bent around in front of the button cell in order to allow for continuous monitoring of the button-cell temperature.

To date, INL has tested a total of seven NASA button cells. Three cells were tested in October 2008, and four were tested in April 2009. Between the two testing periods the testing apparatus was completely rebuilt and expanded, allowing simultaneous testing of two button cells and one stack. All testing was conducted at a furnace temperature of 850°C. Table 5-1 lists the various inlet conditions employed for testing of the cells. Testing of Cell 7 was started with an inlet dew point of 50°C, but it was later increased to 62°C to avoid issues of steam starvation and improve cell performance.

Table 5-1. Cell test conditions.

Cell	H_2 Inlet (sccm)	N_2 Inlet (sccm)	H_2O inlet		Inlet Dew-Point T (°C)
			(sccm)	(mole fraction)	
1	63	350	70	0.14	50
2	60	230	282	0.49	77
3	60	300	110	0.23	60
4	50	350	68	0.15	50
5	50	350	70	0.15	50
6	50	350	68	0.15	50
7	50	350	68/138	0.17/0.35	50/62

Figure 5-3 shows results of a voltage sweep and polarization curve test for NASA Cell 1. The V-I curve and resulting ASR curve are shown in Figure 5-3. The V-I curve is relatively linear for current densities less than 0.6 A/cm^2. The nonlinearity of the V-I curve (and the ASR curve) for higher current densities is indicative of steam starvation. At a current density of 0.6 A/cm^2, the steam utilization was only approximately 20%. Starvation was the result of a relatively low inlet steam flow rate, not high steam utilization. Scatter in the ASR values at low current densities is because of difficulties in accurately measuring extremely low current values.

Figure 5-4 presents the inlet/outlet gas mixture dew point values as well as hydrogen production rates for NASA Cell 1. Two different calculated hydrogen production rates are shown: hydrogen production estimated rate from the difference between outlet and inlet dew points, and hydrogen production rate estimated from the cell current (Faraday's Law). As the cell voltage and current increase, steam is consumed. The measured outlet dew point drops in value while the measurement of hydrogen production rate increases in value. The good agreement between the two independent measurements of hydrogen production rate indicates negligible cell leakage and no cell electrical shorting.

Figure 5-6 and Figure 5-6 show polarization curve and voltage sweep results for NASA cell 3. This test used a higher inlet steam flow rate and thus could sustain a significantly higher current density before becoming steam starved. For this cell and these test conditions, starvation was not noted until current densities in excess of 1.4 A/cm^2, or steam utilizations of 30% and greater. SR values for this cell were roughly the same as for Cell 1.

Test results for cell 5 are found in Figure 5-7. This cell was tested in the newly refurbished testing apparatus. In this case, the voltage sweep extended slightly into the fuel cell range of operation. The lower limit for the voltage sweep was determined by the ability of the power supply to sink the current produced by the cell. The resulting polarization curve remained linear through zero current density, indicating low activation polarization. The average ASR for the sweep was 0.33 Ω·cm^2.

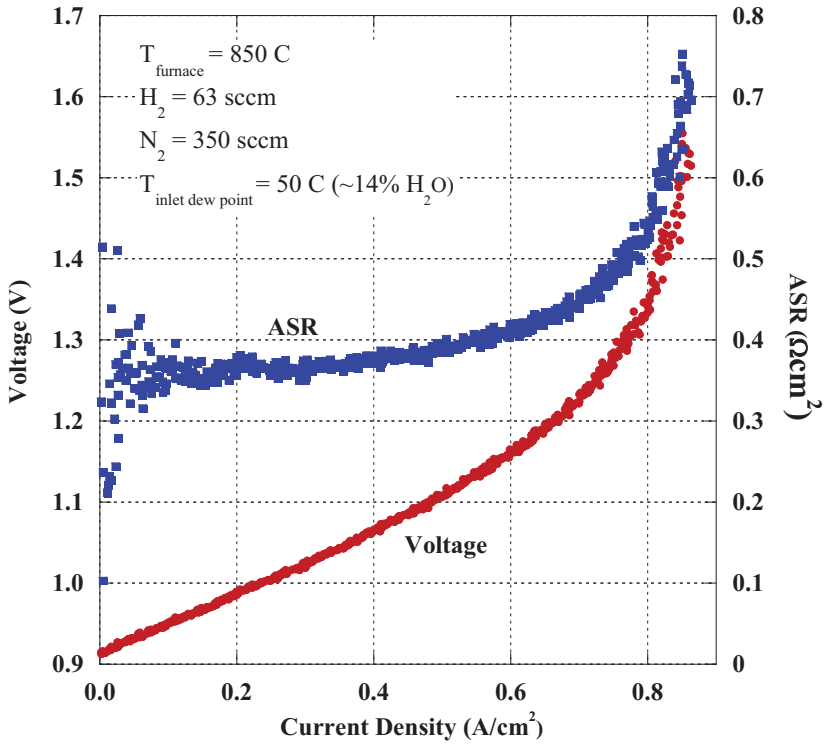

Figure 5-3. Polarization curve for NASA Cell 1.

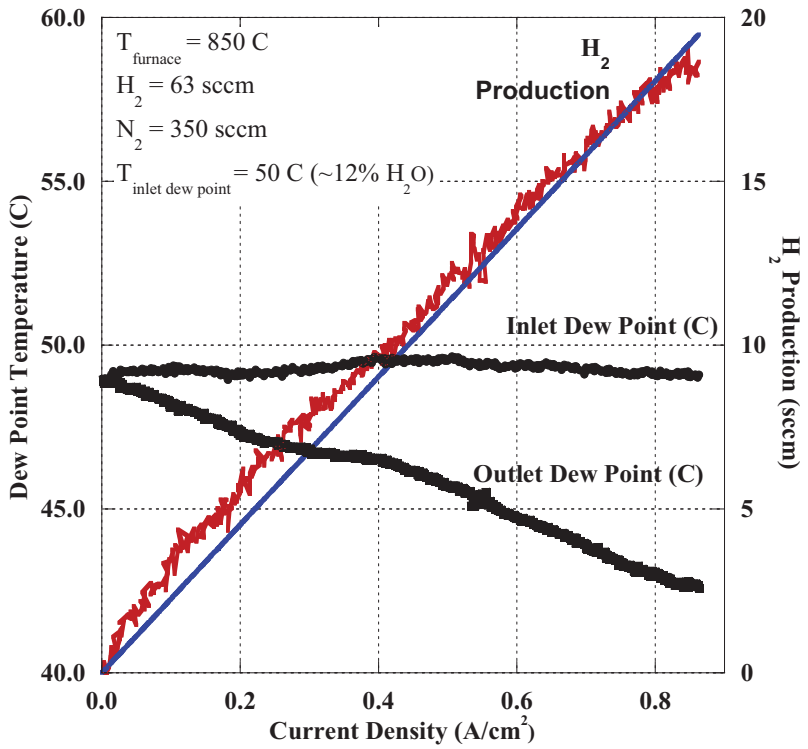

Figure 5-4. H_2 production rates and dew points for NASA Cell 1 (corresponding to Figure 5-3).

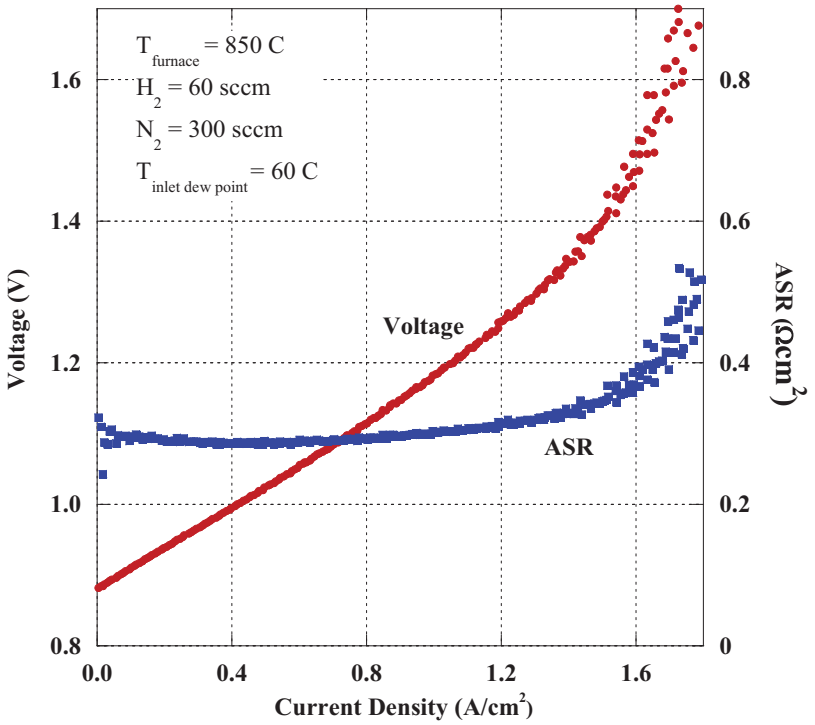

Figure 5-5. Polarization curve and respective ASR values for NASA Cell 3.

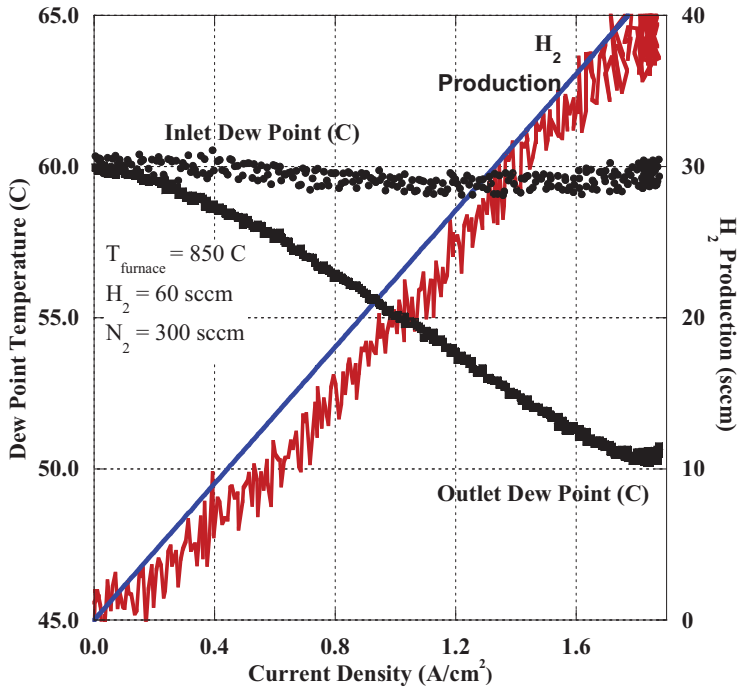

Figure 5-6. H_2 production rates and dew points for NASA Cell 3 (corresponding to Figure 5-5).

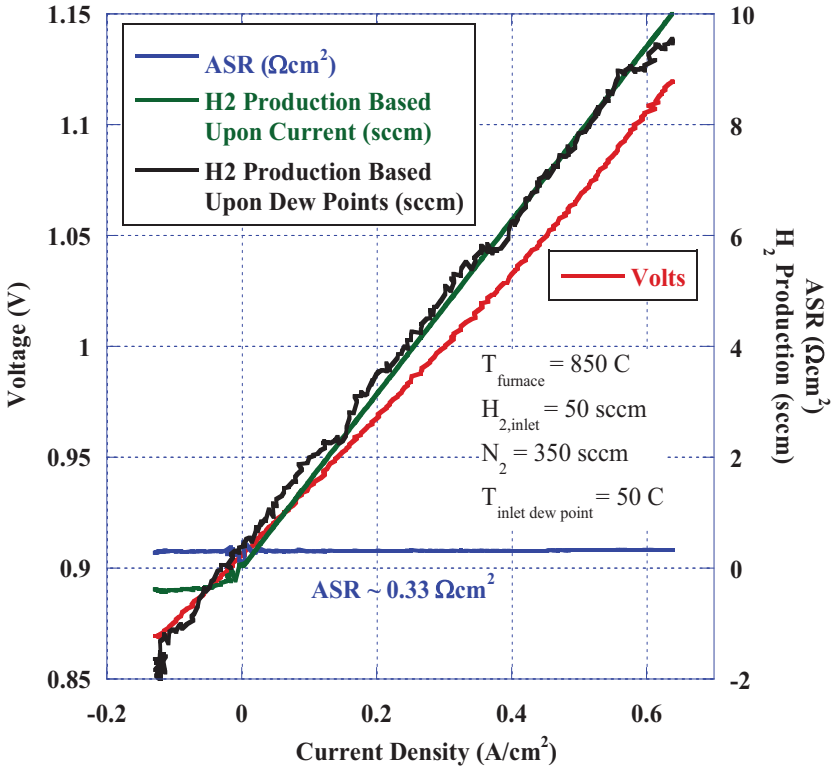

Figure 5-7. H_2 production rates and polarization curve for NASA Cell 5.

NASA Cell 7 was extensively characterized. Two initial voltage sweeps and polarization curve tests were performed, after which the cell operated in a steady state for over 420 hours. During this extended period of operation, three additional voltage sweeps were performed: at 20 hours, 40 hours, and 80 hours elapsed test time. Figure 5-8 summarizes the voltage sweeps. The first sweep was run for an inlet dew point of 50°C, whereas the inlet dew-point temperature for the remaining sweeps was 62°C. Steam starvation was only observed in the first (low inlet dew point temperature) sweep. Comparison of the four subsequent voltage sweep shows that the ASR values gradually deteriorated with time, indicating a slow degradation in cell performance.

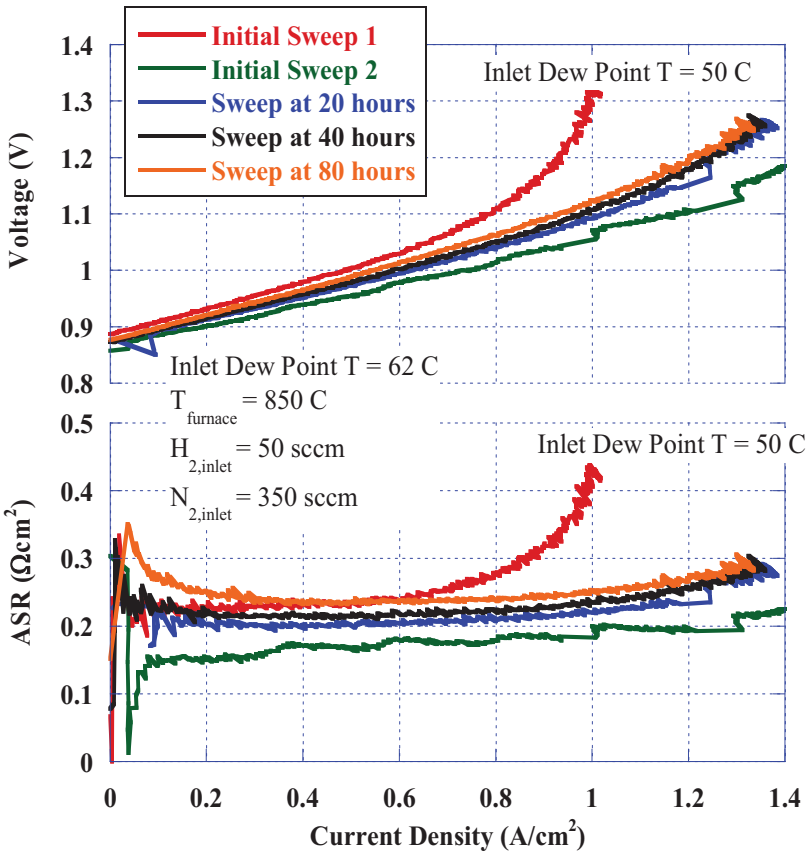

Figure 5-8. Polarization curves for NASA Cell 7.

Figure 5-9 presents the long duration test data for NASA Cell 7. After initial characterization, the cell voltage was set to 1.2 volts and the testing continued for 420 hours. Three voltage sweeps/polarization curves were generated during long duration testing, as indicated on the figure. Three events occurred during long duration testing. At 64 hours, additional heat trace heaters and insulation were added around some valves in the test apparatus. This was done to prevent condensation. It seemed to temporarily improve the cell ASR. At 160 hours elapsed test time, there was a loss of power. Since the computer for the data acquisition system was not powered via an uninterruptible power supply, there was a loss of control. It resulted in cooling the cell furnace from 850 to 700°C. This disruption caused the cell ASR to increase from 0.28 to 0.34 $\Omega \cdot cm^2$. The cell did recover somewhat, but at 235 hours test duration, the computer lost communication with the data acquisition system due to a faulty cable. This again required several hours to repair, during which time the furnace cooled to 550°C. During this period, the cell ASR increased from 0.33 0.4 $\Omega \cdot cm^2$. The loss of power and communication were the dominant contributors to poor cell performance.

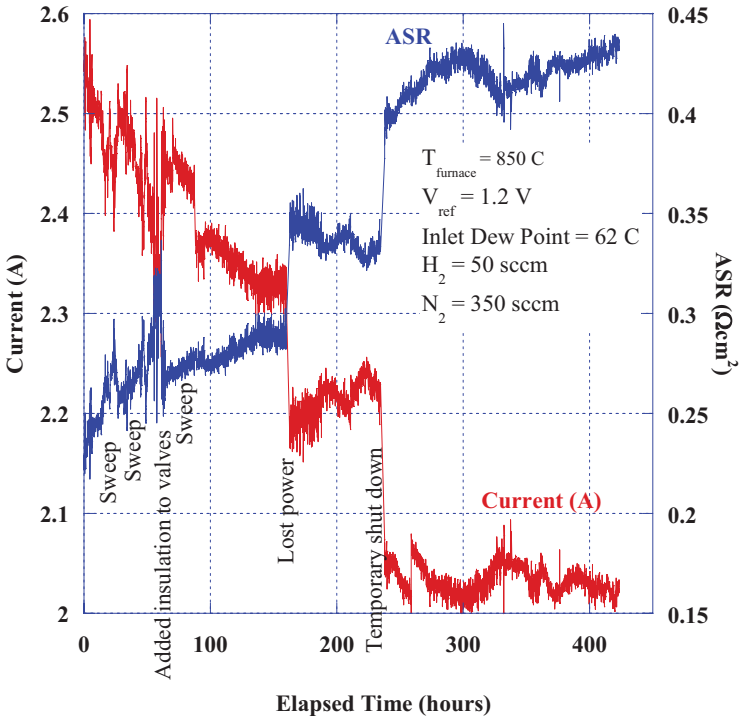

Figure 5-9. Long duration test data for NASA cell 7.

The NASA cells were designed as fuel cells. However, the cells performed quite well as steam electrolyzers. Depending, of course, upon inlet steam flow rate, the cells can handle quite high current densities. Initial performance, as measured by ASR values, was good. More long duration tests are planned for the future to characterize cell degradation.

6. INL TESTS ON DEGRADATION IN SHORT STACKS AND ILS STACKS

O'Brien et al. (2009a and 2009b) recently summarized INL's test results on HTE tests using solid oxide cells, including observations of long-term performance degradation of SOECs. INL cells and stacks utilize scandia-stablized zirconia (ScSZ) electrolyte-supported cells, which do not necessarily represent the state-of-the-art in cell design. The scandia dopant level in these cells was only about 6 mol%, which is not high enough to be considered fully stabilized. In addition, ScSZ with dopant levels less than 10% have been shown to exhibit an aging effect with annealing at 1,000°C (Haering et al. 2005).

Long-term degradation in button cell tests can only be caused by degradation of the electrodes, the electrolyte, or electrode-electrolyte delamination. There are no effects associated with corrosion, contact resistance, flow channels, or interconnects, because these components are not present. The results of a long-term, button-cell test are presented in Figure 6-1. This figure shows the ASR of a button cell plotted as a function of time over the duration of an 1,100-hour test. The ASR increases quite rapidly at the start of the test from an initial value of ~0.6 ohm cm^2 to a value of 0.9 ohm cm^2 over about 40 hours. Between 100 and 1,100 hours, the ASR increases from 0.98 ohm cm^2 to 1.33 ohm cm^2. If the initial 100 hours is considered to be a cell conditioning period, the degradation rate over the following 1,000 hours is about 35%. This is obviously an unacceptable rate of degradation. As a comparison, the Phase-III SECA target degradation rate is 0.1%/1,000 hours. Several companies are currently coming very close to meeting that target in the SOFC mode of operation.

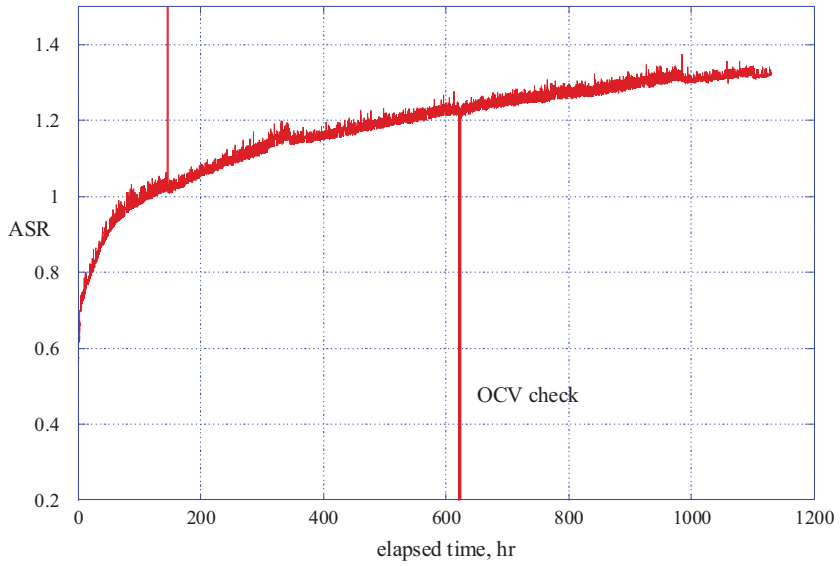

Figure 6-1. Area-specific resistance of a button cell as a function of time for the 1,100-hour test.

Performance degradation results with a 25-cell SOEC stack tested for 1,000 hours at INL were presented by O'Brien et al. (2007) and are shown in Figure 6-2 and Figure 6-3.
Figure 6-2 plots the stack ASR as a function of time for the 1,000 hours. The furnace temperature was increased from 800 to 830°C over an elapsed time of 118 hours, resulting in a sudden drop in ASR. The increase in ASR with time represents degradation in stack performance. The degradation rate decreases with time and is relatively low for the last 200 hours of the test. However, from the 118-hour mark to the end of the test, the ASR increased more than 40% over approximately 900 hours. Reduction of this performance degradation is an objective of ongoing research. Figure 6-3 shows the corresponding generation of hydrogen.

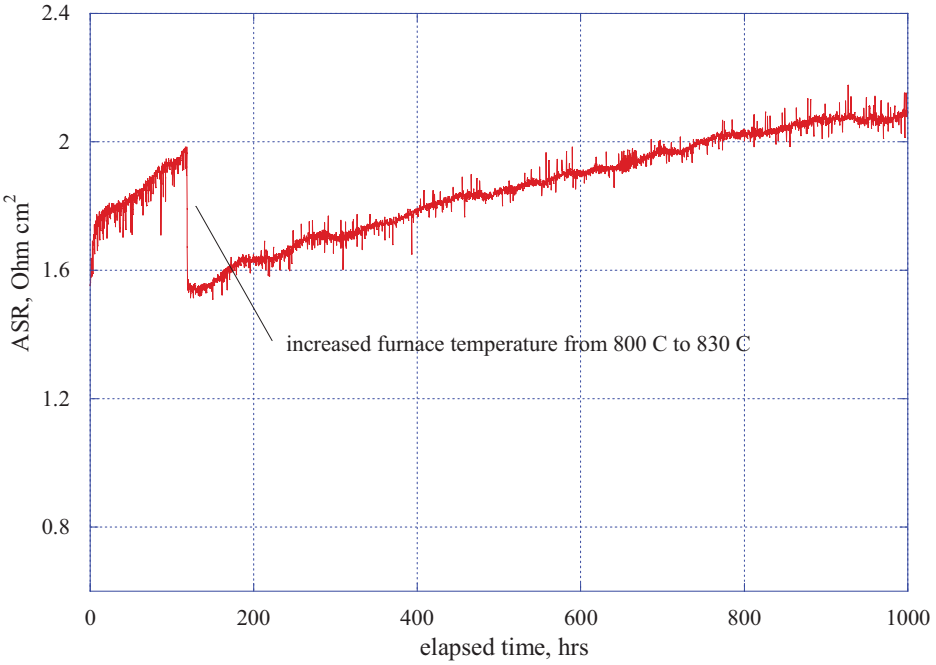

Figure 6-2. Area-specific resistance of a 25-cell stack as a function of time for a 1,000-hour test.

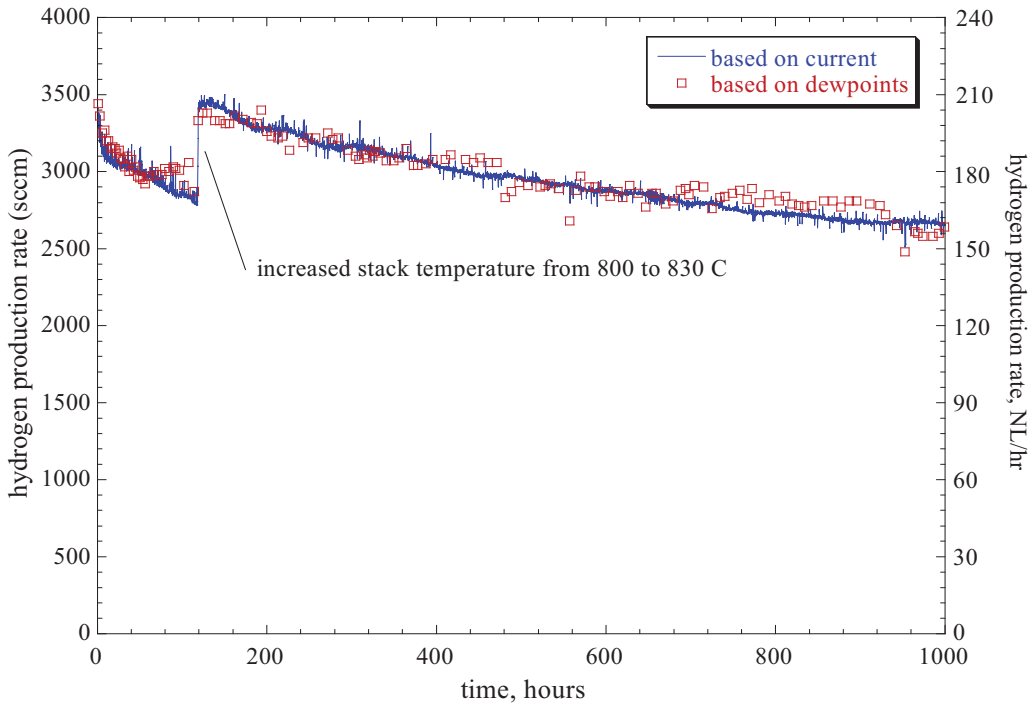

Figure 6-3. Hydrogen production rates during 1,000-hour long-term test.

Performance degradation of the ILS system is documented in Figure 6-4. Over a test period of 700 hours, module-average ASR value increased by a factor of ~5, from an initial value near 1.5 ohm-cm^2. Some of the observed degradation was caused by balance-of-plant issues. For example, prior to about 480 hours of testing, unanticipated condensation occurred in the hydrogen recycle system. It led to erratic control of the hydrogen flow rate because of the intermittent presence of liquid water in the mass flow controllers. This problem led to time periods during which there may have been no hydrogen flow to the ILS stacks, leading to accelerated performance degradation associated with oxidation of the nickel cermet electrodes. A plot of the time history of ILS hydrogen production is given in Figure 6-5. Peak electrolysis power consumption and hydrogen production rate were 18 kW and 5.7 Nm^3/hr, respectively, achieved at about 17 hours of elapsed test time.

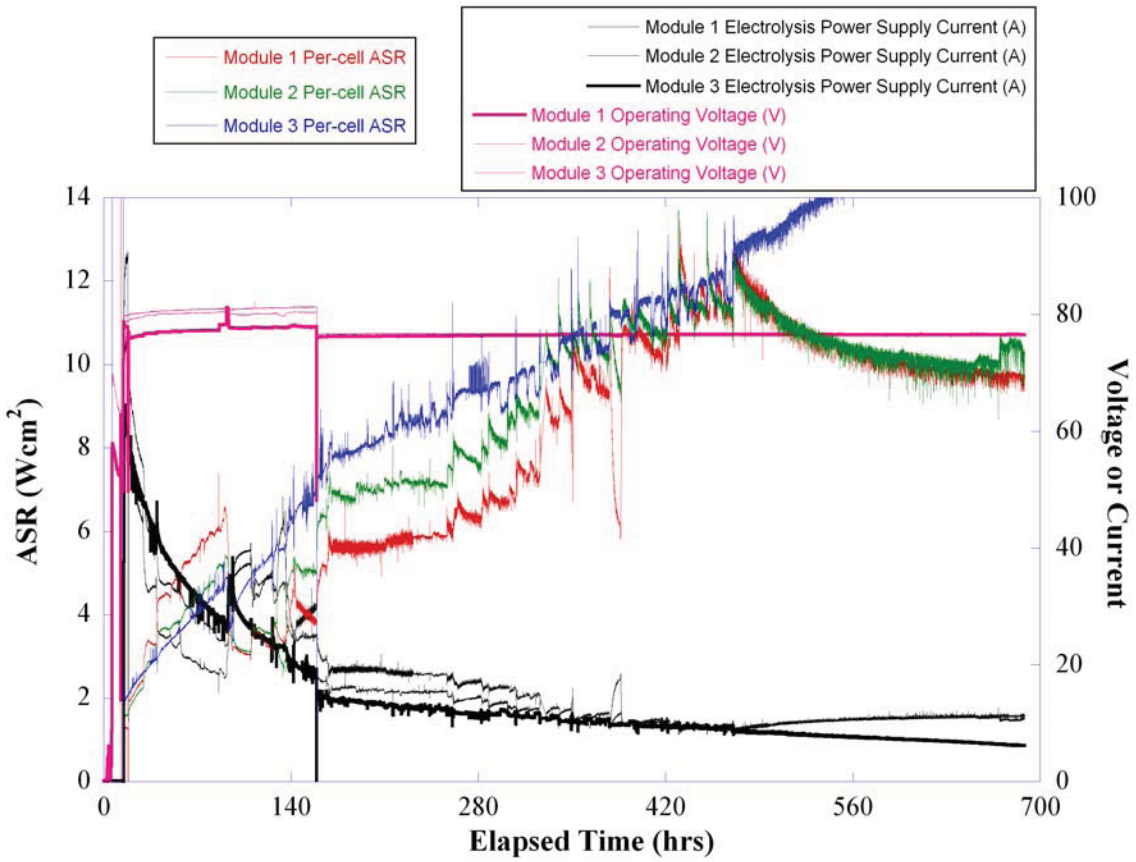

Figure 6-4. Time history of ILS module ASR values, voltages, and current over 700 hours of operation.

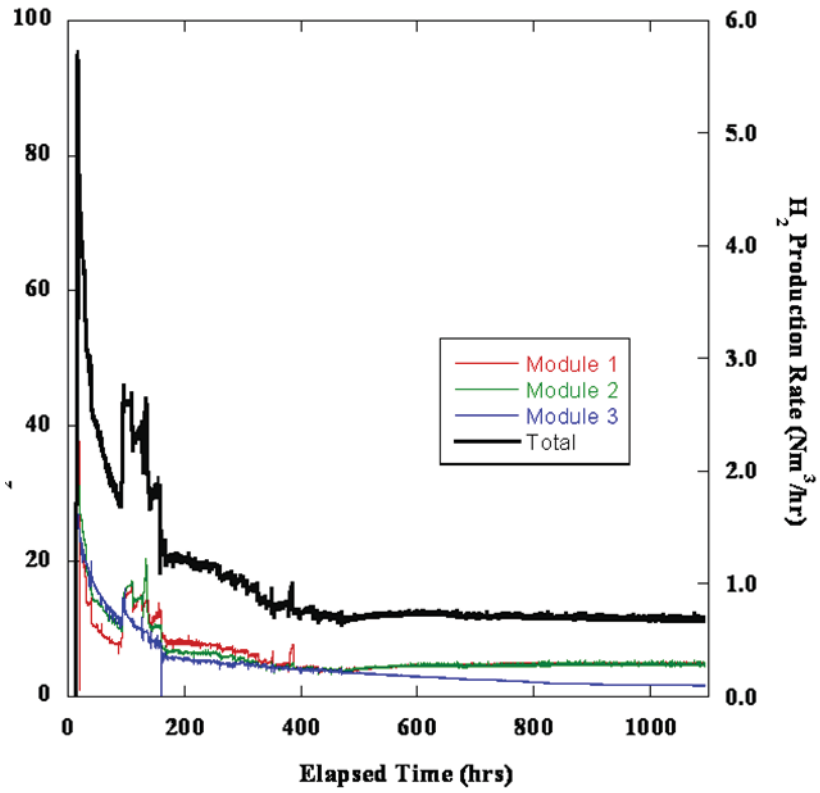

Figure 6-5. Time history of hydrogen production rate in the ILS.

7. IMPROVED CERAMATEC CELLS

The INL ILS cells / stacks were manufactured by Ceramatec Inc.. Figure 4 shows the Ceramatec stack construction. These consisted of a Sc-stabilized zirconia electrolyte (approximately 200 μm thick), nickel cermet hydrogen electrode, and manganite air electrode with a lanthanum strontium chromite (LSC) current distribution layer. Interconnect separator plates were stainless 400 with rare earth scale treatment and a LSC current distribution layer on the air side. The air side flow channel was a corrugated foil of Alloy X with scale treatment and a fired LSC layer. Stainless 400 edge rails were treated with yttria stabilized zirconia (YSZ) coating to inhibit corrosion. The hydrogen-side flow channel was an untreated Ni201 corrugation with nickel felt spot welded to the flow channel.

Post-test evaluation of the cells by the cell manufacturer Ceramatec indicated:

- Hydrogen electrode appeared to be in good condition
- Oxygen electrode showed some delamination with an apparent foreign layer deposited at the electroyte interface.

These cells were also examined by Argonne National Laboratory and the Massachusetts Institute of Technology. Their analysis showed that the O_2-electrode delaminated from the electrolyte near the edge. One possible reason for this delamination is excessive pressure buildup due to high O_2 flow in the over-sintered region. Furthermore, electrochemical reactions were also identified as a cause of degradation. Two important degradation mechanisms were examined: (1) transport of Cr-containing species from steel interconnects into the oxygen electrode and LSC bond layers in SOECs, and (2) cation segregation and phase separation in the bond layer.

These post-test examinations prompted Ceramatec to develop a new oxygen-side electrode composition. Second in priority, Ceramatec also began development of a fully-stabilized Sc-zirconia electrolyte material. The new oxygen-side electrode was first tested at the INL as a 10-cell stack to fulfill a 2500 hour long-duration test milestone. The fully-stabilized electrolyte concept was first tested at the INL as a button cell.

8. STATUS OF 2500-HR TEST OF A 10-CELL CERAMATEC STACK

In May of 2009, Ceramatec delivered to the INL a 10-cell stack incorporating a new, improved oxygen-side electrode material. It is hoped that this proprietary electrode material will result in improved (lower) degradation rates. Preliminary testing at Ceramatec with other stacks incorporating this electrode material indicated lower initial performance (higher initial ASR), but also much lower degradation rates. It was decided to use this stack for a 2500 hour long duration test scheduled for FY09. Heat-up and testing began at 4:26 PM on May 27, 2009. This test remains in progress as of the time of writing for this report. Figure 29 presents a time history of operating voltage, current, and per-cell ASR for this stack.

The data acquisition and control system for this test was configured to feedback control the stack power supply such that the stack operating voltage is always at thermal neutral. The stack operating conditions were thus kept constant at 12.9 V, T_{stack} = 800 C, N_2 = 1600 sccm, inlet H_2 = 800 sccm, and $T_{dp,\ inlet}$ = 80 C. To date, the stack has run continuously for 1800 hours. The stack exhibited an initial rapid degradation of approximately 10%, based upon ASR. Beyond about 100 hours elapsed test time, the ASR degraded from 2.3 Ωcm^2 to 2.6 Ωcm^2. Ignoring the first 100 hours, this corresponds to a degradation rate of 7.7%/1000 hours.

Several events disrupted the steady-state testing. It is not clear whether these events affected the long-term performance of the stack. Most of these disruptions involved interruptions of inlet gas flows (N_2 and H_2), caused by problems with the gas mass flow controller electronics. Later in testing (beyond 1200 hours), the gas sparger in the gas humidifier would become periodically clogged, also interrupting gas flows to the stack. Several analog pressure gauges were installed to monitor the sparger back pressure such that it could be unclogged before gas flow was interrupted.

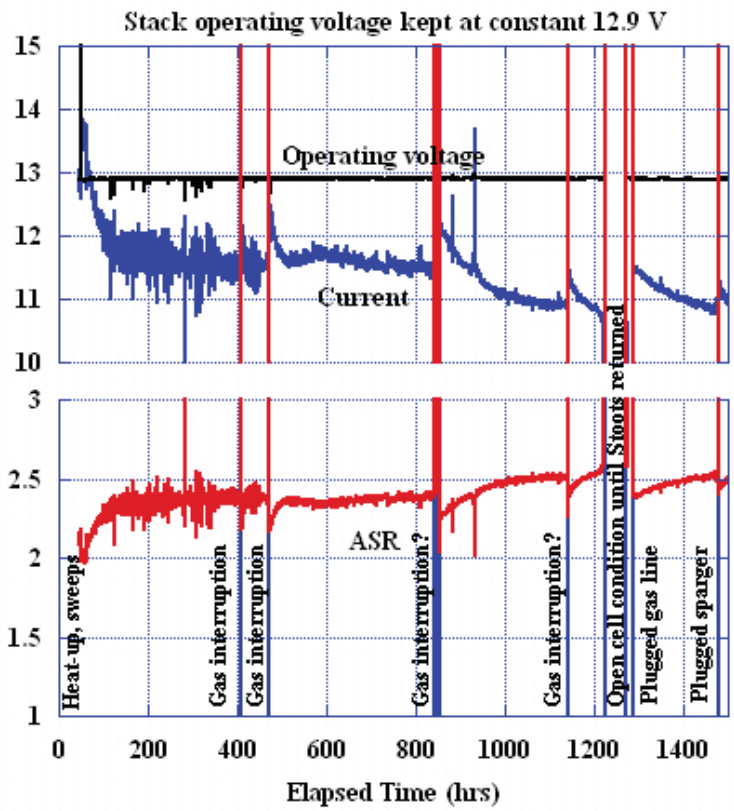

Figure 8-1. Performance of the 10-cell Ceramatec stack through 1,500 hours.

9. STATUS OF CERAMATEC FULLY-STABILIZED ELECTROLYTE BUTTON CELL TEST

On July 25, 2009, long duration testing began of a fully-stabilized electrolyte button cell from Ceramatec. This cell had the traditional oxygen-side electrode, rather than the more advanced electrode material used in the 2500 hour test. **Error! Reference source not found.** is a complete test history to date for this button cell. At 64 hours elapsed test time, the electrolysis power supply was switched from constant output to feedback control based upon the cell operating voltage. At this time, the cell operating voltage was set to thermal neutral (1.29 V). The cell degraded quite quickly, as can be seen from the ASR curve in **Error! Reference source not found.**. This seems to indicate that the primary explanation for cell degradation in electrolysis mode of operation involves the oxygen side electrode. Future plans call for testing another advanced cell made up of a fully stabilized electrolyte with the advanced oxygen-side electrode material.

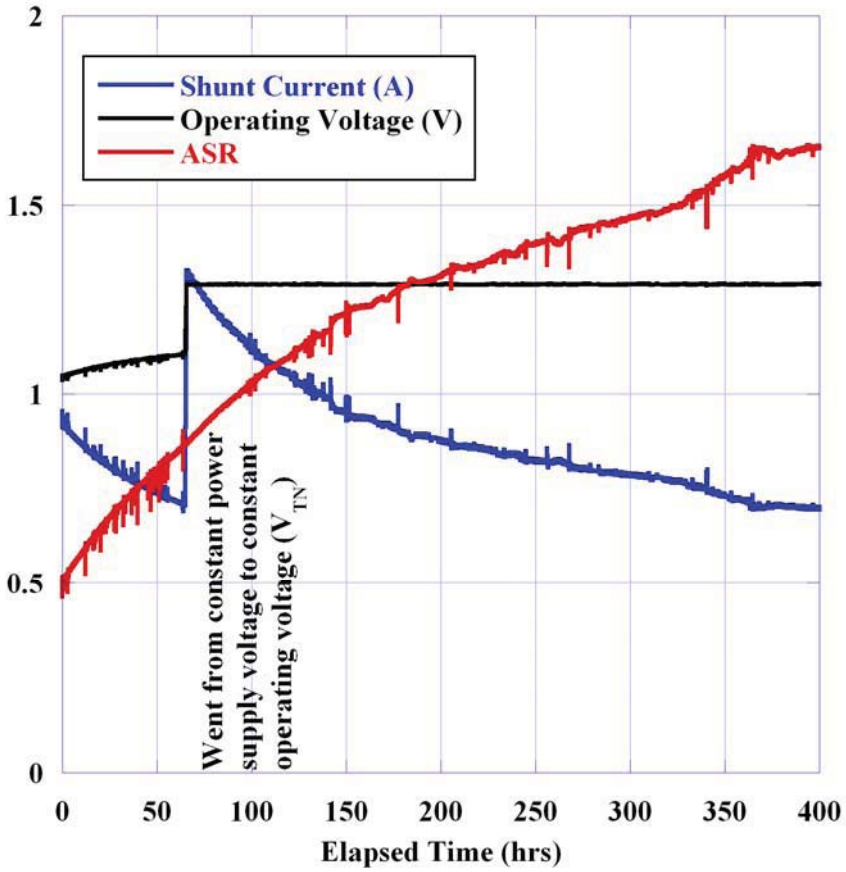

Figure 9-1. Performance of the Ceramatec fully-stabilized electrolyte button cell.

10. ACKNOWLEDGMENTS

This work was supported by the U.S. Department of Energy, Office of Nuclear Energy, Nuclear Hydrogen Initiative Program. The Idaho National Laboratory is operated for the U.S. Department of Energy's Office of Nuclear Energy by the Battelle Energy Alliance under contract number DE-AC07-05ID14517.

11. REFERENCES

Akkaya, A. V., 2007, "Electrochemical Model for Performance Analysis of a Tubular SOFC," *Int. J. Energy Research*, 31, 79–98.

Carter, D. J. et al., 2008, "Determining Causes of Degradation in High Temperature Electrolysis Stacks," *Workshop on Degradation in Solid Oxide Electrolysis Cells and Strategies for its Mitigation, Fuel Cell Seminar & Exposition, Phoenix, AZ, October 27, 2008*.

Gazzarri, J. I., 2007, "Impedance Model of a Solid Oxide Fuel Cell for Degradation Diagnosis," Ph. D. Thesis, University of British Columbia, Vancouver, Canada.

Gemmen, R. S., Williams, M. C., and Gerdes, K., 2008, "Degradation Measurement and Analysis for Cells and Stacks," *J. Power Sources*, 184, 251–259.

Guan, J. et al., 2006, "High Performance Flexible Reversible Solid Oxide Fuel Cell," *GE Global Research Center Final Report for DOE Cooperative Agreement* DE-FC36-04GO-14351.

Haering, C., Roosen, A., Schichl, H., and Schnoller, M., 2005, "Degradation of the electrical conductivity in stabilized zirconia system Part II: Scandia-stabilised zirconia," Solid State Ionics, 176, 3–4, 261-268.

Hartvigsen, J. J., Larson, D., and Elangovan, S., 2009, "Post Test Stack Disassembly of Stacks A and B from Module #3 from the Full Scale ILS Test in the 4th Quarter 2008," Ceramartec Progress Report to INL for Subcontract 83664.

Hauch, A., 2007a, "Solid Oxide Electrolysis Cells – Performance and Durability," Ph.D. Thesis, Technical University of Denmark, Risø National Laboratory, Roskilde, Denmark.

Herring, J. S., Stoots, C. M., O'Brien, J. E., Hartvigsen, J. J., and Housley, G., 2007, "Recent Progress in High Temperature Electrolysis," AIChE Meeting, Salt Lake City, UT, November 5–9, 2007.

Ivers-Tiffée, E. and Virkar, A. V., 2003, "Electrode Polarisation," Chapter 9 in *High Temperature Solid Oxide Fuel Cells: Fundamentals, Design and Applications*, Edited by Singhal, S. C. and Kendall, K., Elsvier, Oxford, U.K.

Ni, M., Leung, M. K. H., and Leung, D. Y. C., 2006, "A Modeling Study on Concentration Overpotentials of a Reversible Solid Oxide Fuel Cell," *J. Power Sources*, 163, 460–466.

O'Brien, J. E., Stoots, C. M., Herring, J. S., and Hartvigsen, J. J., 2007, "Performance of Planar High-Temperature Electrolysis Stacks for Hydrogen Production from Nuclear Energy," *Nuclear Technology*, 158, 118–131.

O'Brien, J. E., Stoots, C. M., Herring, J. S., Condie, K. G., and Housley, G. K., 2009a, "The High-Temperature Electrolysis Program at the Idaho National Laboratory: Observations on Performance Degradation," High Temperature Water Electrolysis Limiting Factors, Eifer, Karlsruhe, Germany, June 9-10, 2009.

O'Brien, J. E., McKellar, M. G., Harvego, E. A., and Stoots, C. M., 2009b, "High-Temperature Electrolysis for Large-Scale Hydrogen and Syngas Production from Nuclear Energy – system Simulation and Economics," International Conference on Hydrogen Production, ICH2P-09, Oshawa, Canada, May 3-6, 2009.

Sohal, M. S., 2009a, "Degradation in Solid Oxide Cells during High Temperature Electrolysis," Idaho National Laboratory Report INL/EXT-09-15617.

Sohal, M. S., O'Brien, J. E., Stoots, C. M., Herring, J. S.,Hartvigsen, J. J., Larsen, D., Elangovan, S., Carter, J. D., Sharma, V. I., and Yildiz, B., 2009b, "Long-Term Degradation Testing of High-Temperature Electrolytic Cells," Idaho National Laboratory Report INL/EXT-09-16004.

Stoots, C. M., Condie, K. G., O'Brien, J. E., and Housley, G., 2009a, "Integrated Laboratory Scale Test Report," Idaho National Laboratory Report INL/EXT-09-15283.

Virkar, A. V., 2007, "A Model for Solid Oxide Fuel Cell (SOFC) Stack Degradation," *J. Power Sources*, 172, 713–724.

Windisch, C. F., Stevenson, J. W., Simner, S. P., Williford, R. E., and Chick, L. A., 2002, "Experimentally-Calibrated Spreadsheet-based SOFC Unit-Cell Performance Model," Pacific Northwest National Laboratory, PNNL-SA-37014, presented at *2002 Fuel Cell Seminar: Fuel Cells-Reliable, Clean Energy for the World, Palm Springs, CA, November 21, 2002*.